

## 18. VIVISECTION AND AUTOPSY OF ACTIVE AND FOSSIL HYDROTHERMAL ALTERATIONS OF BASALT BENEATH AND WITHIN THE TAG HYDROTHERMAL MOUND<sup>1</sup>

José J. Honnorez,<sup>2</sup> Jeffrey C. Alt,<sup>3</sup> and Susan E. Humphris<sup>4</sup>

### ABSTRACT

The TAG (Trans-Atlantic Geotraverse) active hydrothermal mound is 30–40 m thick and consists of 4 to  $5 \times 10^6$  tons of pyrite-, quartz-, and anhydrite-rich breccias. A vertically and laterally zoned stockwork, approximately 100 m in diameter, extends at least 125 m below the mound surface. Petrographic and mineralogic studies of core drilled during ODP Leg 158 were used to reconstruct the sequence of alteration processes of crustal rocks beneath and within the mound. The first stage of hydrothermal alteration is the chloritization of the basaltic basement beneath the mound as a result of interaction with Mg-bearing hydrothermal solutions, which are different from the “zero” Mg fluids presently discharged by the Black Smoker Complex, near the center of the TAG mound. In the deepest part of the stockwork underlying the central part of the mound, the basalt is almost completely chloritized (with minor quartz and pyrite) and Cr-spinel is the only primary mineral left. Beneath the mound margins, the chloritization process is restricted to millimeter- to centimeter-thick halos parallel to the exposed surfaces of basalt fragments. Chloritization occurred at temperatures ranging from 250°–370°C. Chlorite under the southeast mound margin is Mg-rich and formed via reaction with heated seawater (Alt and Teagle, Chap. 21, this volume; Teagle et al., Chap. 22, this volume). Chlorite under the northwest margin of the mound and in the deep chloritized stockwork is poorer in Mg and formed from black smoker-like hydrothermal fluids mixed with small amounts of seawater. The second stage of hydrothermal alteration is the replacement of basalt and chloritized basalt by paragonite + quartz + pyrite. At this stage, all of the primary minerals are replaced. Paragonite formed via replacement of chlorite in the stockwork samples and as a result of direct precipitation from hydrothermal fluids in interstitial spaces of the quartz + pyrite breccias. Paragonite is often Cr-rich. Na-rich micas reflect the high Na/K ratio of the present day hydrothermal fluids discharged by the TAG black smokers at temperatures of up to 360°C. As a result of the recurrent silicification and pyritization, basaltic minerals and textures are progressively obliterated and completely replaced by mixtures of “dirty” quartz + pyrite with interstitial paragonite, which is extremely difficult to distinguish from the directly precipitated quartz + pyrite + paragonite assemblage. The last stage of hydrothermal mineralization consists of anhydrite precipitation in open spaces such as veins and voids in the breccias. Finally, the basement under the mound margins that are already displaying the first stage of chloritization is affected by low-temperature alteration by cold oxygenated seawater. Intensely altered basalt clasts are found within the mound breccias at much shallower depths above than that expected for the top of the basement. Three mechanisms are tentatively proposed to explain this observation: (1) high velocity entrainment in hydrothermal fluid, (2) volume expansion during alteration and mineralization in a process analogous to “frost jacking” and “frost heave”; the volume expansion process could proceed via the formation of quartz + pyrite, or by repeated precipitation and dissolution of anhydrite in veins and pore spaces, or (3) nearly complete replacement of a volcanic mound by hydrothermal alteration products. The third mechanism implies that the hydrothermal mound was superimposed upon and replaced a volcanic edifice.

### INTRODUCTION

Whereas our knowledge of the reactions occurring at depth in submarine hydrothermal systems has increased greatly in recent years (Alt, 1995; Seyfried and Ding, 1995; Von Damm, 1995), very little is known about hydrothermal upflow zones within ocean crust. Reactions in shallow upflow zones and feeder zones for seafloor massive sulfide deposits may be pervasive and thus significant, in that up to about 90% of the heat flux from axial hydrothermal systems occurs via low temperature diffuse flow, which is thought to arise from reactions in the shallow subsurface (Rona and Trivett, 1992; Schultz et al., 1992).

Chloritization, sericitization, silicification, and pyritization are well-known alteration features associated with land-based volcanogenic massive sulfide (VMS) ore deposits related to ophiolites and other submarine and non-oceanic contexts (e.g., submarine pedestals

of active volcanoes at shallow depths). Stockwork-like sulfide mineralization associated with hydrothermal alteration silicates (i.e., chlorite, actinolite, epidote, albite, quartz) are known from samples dredged from oceanic fracture zones (Bonatti et al., 1976) or from drilled cores (i.e., Hole 504B; Honnorez et al., 1985). Hydrothermal quartz-pyrite breccias were also recovered by dredging and submersible from fracture zones and faults (Mottl, 1983; Delaney et al., 1987; Saccocia and Gillis, 1995). In these cases, quartz + sulfide veins and associated chlorite were ascribed to upflow zones of subseafloor hydrothermal systems and could be considered submarine analogues of similar features beneath VMS deposits.

Sericitization of rocks associated with seafloor sulfide deposits appears to be rare (Alt et al., 1987; Alt and Jiang, 1991), but high-temperature (350°C) Al-smectitic alteration may be a similar or analogous process (Embley et al., 1988; Haymon and Kastner, 1986). Other alteration zones resulting from processes such as propylitization, saussuritization, and various types of argilic alterations are commonly observed in land-based sulfides ore deposits (Richards et al., 1989), but have not been found yet in the oceanic crust. This is because the stockwork and feeder zones immediately underlying seafloor hydrothermal massive sulfide deposits have only rarely been sampled from present-day oceanic crust.

In contrast to focused upflow that forms seafloor sulfide deposits, diffuse upflow zones occur where upwelling hydrothermal fluids mix with seawater in the subsurface. In these cases, sulfides  $\pm$  quartz are

<sup>1</sup>Herzig, P.M., Humphris, S.E., Miller, D.J., and Zierenberg, R.A. (Eds.), 1998. *Proc. ODP, Sci. Results.*, 158: College Station, TX (Ocean Drilling Program).

<sup>2</sup>CNRS-Centre de Géochimie de la Surface, Université Louis Pasteur, 1 rue Blessig, 67084 Strasbourg Cedex, France. honnorez@illite.u-strasbg.fr

<sup>3</sup>Department of Geological Sciences, 2534 C.C. Little Building, The University of Michigan, Ann Arbor, MI 48109-1063, U.S.A.

<sup>4</sup>Department of Geology and Geophysics, Woods Hole Oceanographic Institution, Woods Hole, MA 02543, U.S.A.

deposited within the crust, and only the cooler, diluted, and mixed hydrothermal fluids reach the seafloor (Edmond et al., 1979; Honnorez et al., 1985; Alt, 1995). This type of mineralization is typical of ophiolites (Harper et al., 1988; Alt, 1994).

Our knowledge of the deep portions of hydrothermal upflow zones only comes from ophiolites, where epidiosites (epidote + quartz + titanite rocks), are thought to indicate the root zones of upflow zones at the base of the sheeted dyke complex (Richardson et al., 1987; Schiffman et al., 1987; Harper et al., 1988; Nehlig et al., 1994). Such rocks have not been found in present day oceanic crust, however. In ophiolites, the epidiosites are thought to give way upward to quartz + epidote and quartz sulfide veins, which represent hydrothermal upflow zones (Nehlig et al., 1994).

In the fall of 1994, Leg 158 of the Ocean Drilling Program carried out a program of drilling into the TAG hydrothermal mound, a large seafloor massive sulfide deposit with actively venting black smokers. Drilling penetrated to 126 mbsf and defined the stockwork feeder zone for the deposit. This paper presents the results of a mineralogical, petrographic, and geochemical study of the different alteration processes that affected (and are probably still affecting) the basaltic basement rocks under and within the TAG active hydrothermal mound.

## GEOLOGICAL SETTING OF THE TAG HYDROTHERMAL FIELD AND ACTIVE MOUND

The geologic setting of the TAG mound has been reviewed recently by Rona et al. (1993) and Humphris, Herzig, Miller, et al. (1996), and is briefly summarized here. The TAG hydrothermal field is located at 26°N on the Mid-Atlantic Ridge, and covers an area of 5 × 5 km near a salient at the base of the east wall of the median valley (Fig. 1). Low-temperature hydrothermal activity, with Mn-oxide and nontronite deposits, occurs at 2400–3100 m on the east wall (Fig. 1). Inactive sulfide deposits, which are recrystallized and partly oxidized, occur in two zones on the lower east wall northwest of the active TAG mound (the *Mir* and *Alvin* zones in Fig. 2). U/Th dating suggests that these relict deposits range from 5 × 10<sup>3</sup> to 14 × 10<sup>3</sup> years old (Lalou et al., 1995).

The active TAG mound is located at 26°8'N, 44°49'W at a water depth of about 3600 m (Fig. 1). It lies 1.5–2.0 km east of the spreading axis, on crust that is at least 100 × 10<sup>3</sup> years old. The mound is roughly circular, about 200 m in diameter and 30–50 m high (Fig. 2; Kleinrock et al., 1996). In plan the mound is asymmetric with a cluster of chalcopyrite + anhydrite-rich black smoker chimneys discharging hydrothermal fluids at temperatures of up to 368°C located on top of a 10–15 m high, 20–30 m diameter cone to the NW of the center of the mound (Fig. 2). The Black Smoker Complex is surrounded by an upper terrace at ~3644 m and a lower terrace to the SE at ~3650 m. The Kremlin area on the lower terrace comprises a complex of small (1–2 m) sphalerite-rich white smokers. These emit 260–300°C fluids, which are interpreted to be derived from black smoker-type fluids formed by a combination of cooling, mixing with seawater, and reactions within the mound (precipitation of pyrite, chalcopyrite, and anhydrite, dissolution of sphalerite; Edmond et al., 1995; Tivey et al., 1995; Mills and Elderfield, 1995). Steep slopes on the west, north, and east sides of the upper terrace are the result of mass wasting, which has exposed material rich in silica (quartz and amorphous silica) ± pyrite ± Fe-oxyhydroxides (Tivey et al., 1995).

Diffuse flow of low-temperature (up to 50°C) fluids occurs through much of the surface of the mound and the surrounding sediment apron, which consists of mixtures of pelagic sediment and hydrothermal detritus and precipitates (Becker and Von Herzen, 1996; Mills et al., 1996). In other areas (e.g., the northwest side of the mound), low heat flow suggests recharge of seawater into the mound (Becker and Von Herzen, 1996).

A near-bottom magnetic survey over the TAG mound indicates a magnetic low that lies directly beneath the deposit (Tivey et al., 1993). This has been interpreted as a cylindrical alteration pipe, possibly dipping to the south, that marks the shallow hydrothermal upflow zone (Tivey et al., 1993). The intersection of axis-parallel faults with transverse or oblique faults may influence the location of the TAG deposit (Karson and Rona, 1990; Kleinrock et al., 1996). Reactivation of such faults may help explain the long duration of hydrothermal activity at the TAG deposit: U/Th dating of samples from the TAG mound suggests that hydrothermal activity has occurred there episodically over a period of 40,000–50,000 years (Lalou et al., 1995).

## ALTERATION LITHOSTRATIGRAPHY

The lithostratigraphy of the TAG mound and underlying stockwork and basaltic basement (see Fig. 3) was reconstructed from the 17 holes drilled in 5 general locations (TAG-1 to TAG-5 areas) during Leg 158 and from observation during various submersible dives (Fig. 3). For the purpose of this alteration study the lithostratigraphy will be presented from the sides of the mound inward and bottom upward: that is, from the least altered basement rocks, or the farthest core samples (Hole 957B of TAG-2 area and Hole 957M of TAG-4 area) with respect to the upflow zone of hydrothermal fluids near the center of the mound, then to the most altered rocks beneath the central part of the mound (Holes 957E and C of TAG-1 area) and moving upward from the deepest and most altered samples).

### Alteration Lithostratigraphy at Mound Margins

#### *Holes 957B (TAG-2 area) and 957M (TAG-4 area)*

Hole 957B in the southeastern (TAG-2) area reached basaltic basement at 3672 mbsf, whereas such basement was reached at a somewhat deeper level, 3687 mbsf, in Hole 957M on the western margins of the mound (TAG-4 area). Kleinrock et al. (1996) give the seafloor regional depth as 3680 mbsf for the western and northern portions of the mound margin, and 3660–3670 mbsf for its southern and eastern portions. The 10- to 20-m difference of altitude between the north and west, and south and east margins of the mound, respectively, corresponds to a 11% to 22% slope of the seafloor beneath the mound. Based on the bathymetric map of Kleinrock et al. (1996), we have taken the water depth of the top of the mound upper terrace as 3652 m. As a consequence, the top of Holes 957B in TAG-2 area is 7 m deeper than that of Holes 957M in the TAG-4 area.

Hole 957B is located on the lower terrace of the mound between the Kremlin white smoker field (about 60 m southeast of the Black Smoker Complex) and only 20 m away from the eastern edge of the lower terrace, hence of the mound. The hole was drilled from a depth of 3652 mbsf and penetrated down to nearly 30 m with a recovery of 5.5%. In the lowermost 10 m of the hole, relatively weakly altered basalt fragments and totally chloritized pillow breccias were recovered, along with one piece of red-gray quartz containing a few millimeter-sized chloritized glass shards. From about 20 mbsf to the top of the hole (with a no-recovery hiatus between 15 and 10 mbsf) a few pieces of massive, porous pyrite and pyrite breccia were recovered. The top 10 m of the hole corresponds to 1 m of recovered drill cuttings, with a few pieces of porous, massive sphalerite and massive granular pyrite. One should keep in mind that Hole 957B recovered only a little, and highly disturbed, material.

Hole 957M is situated only 30 m west of the Black Smoker Complex, 20 m from the western edge of the upper terrace. The hole was started from a depth of 3645 mbsf and penetrated 51.2 m with a recovery of 13.6%. Four dark gray fragments of pillow basalt displaying variously colored 0.1- to 1-cm-thick alteration zones were recovered from the bottom of the hole at 3696 mbsf to a depth of 42.5 mbsf.

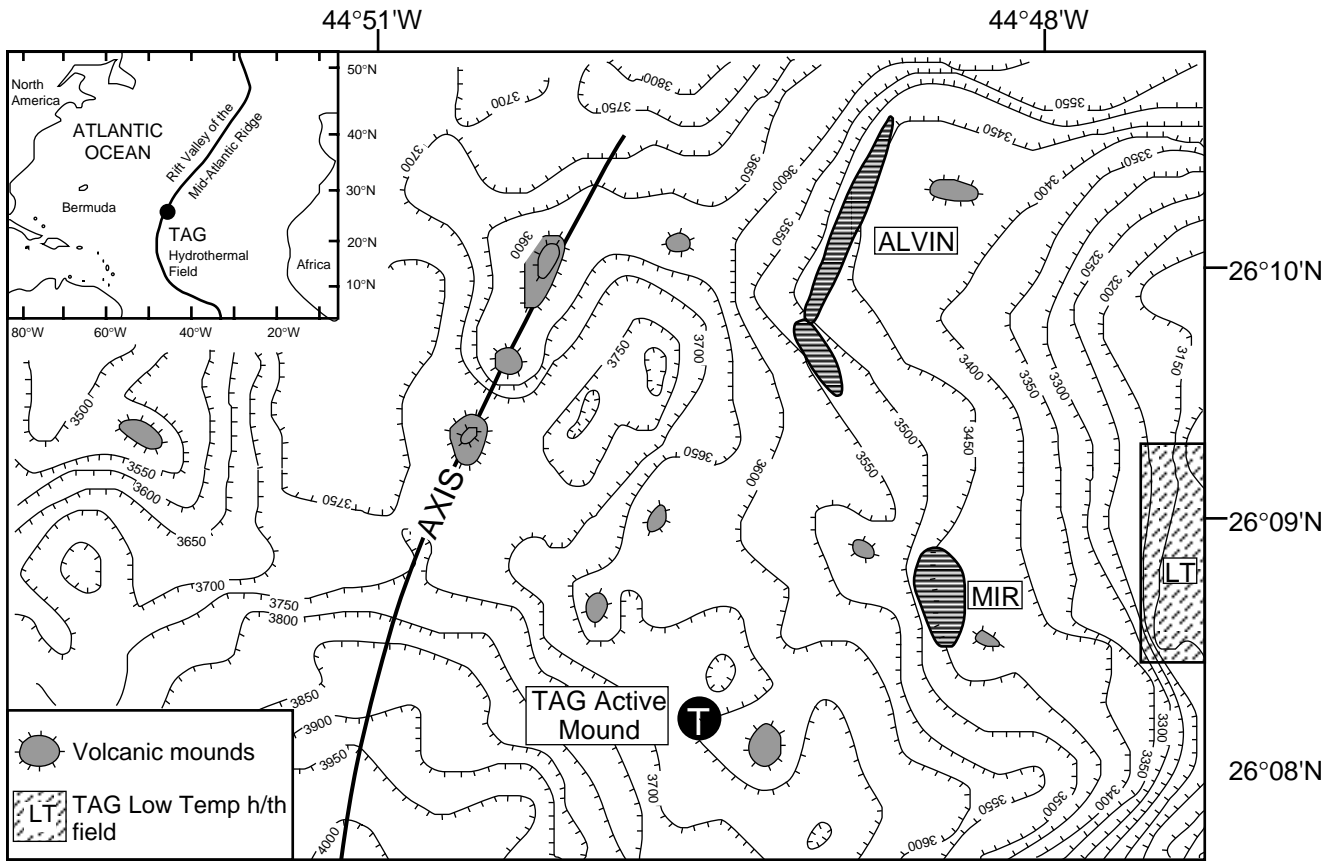


Figure 1. General bathymetric map of the Mid-Atlantic Ridge in the TAG hydrothermal field with the locations of the active hydrothermal TAG mound, the low temperature hydrothermal TAG site, and the inactive hydrothermal *Alvin* and *Mir* mounds.

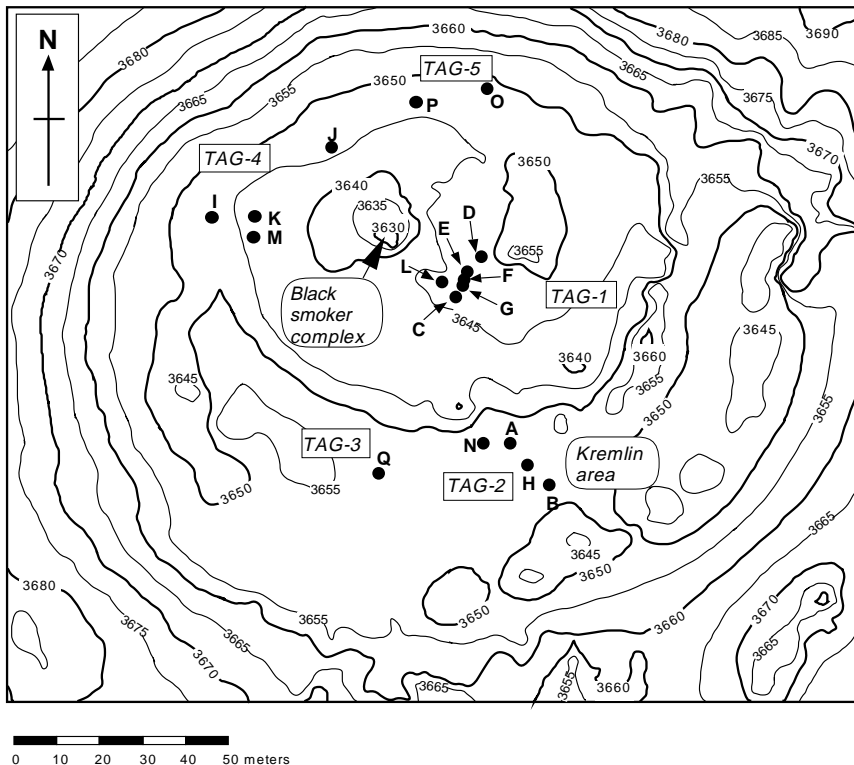


Figure 2. Bathymetric map of the active hydrothermal TAG mound with the locations of the 17 holes drilled during ODP Leg 158 (after Kleinrock et al., 1996).

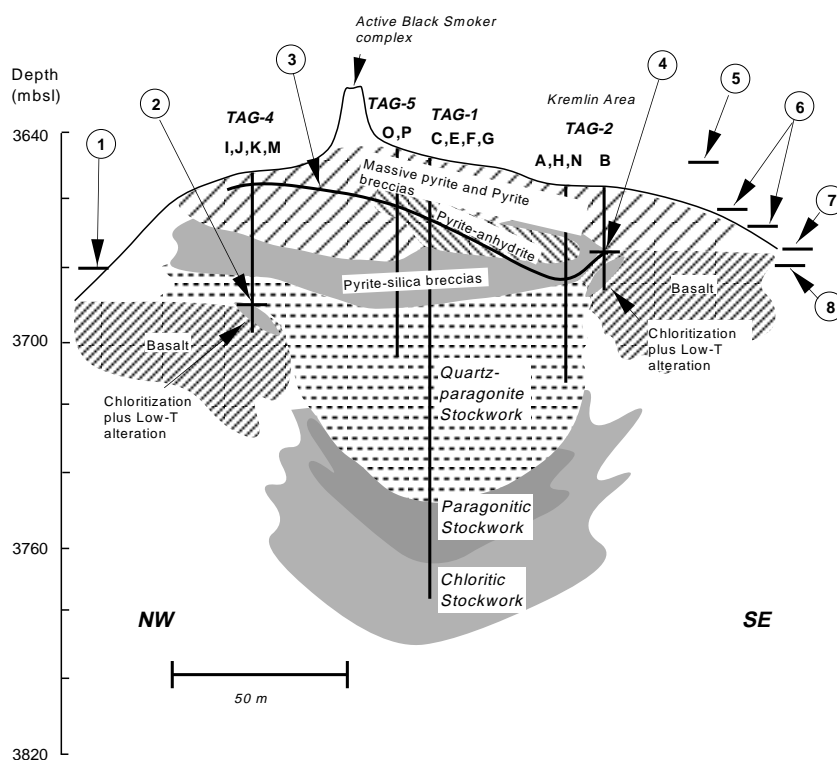


Figure 3. Reconstructed cross section through the TAG mound, its stockwork, and basement. Key: (1) regional depth of the seafloor west and north of the mound at 3680 mbsl (Kleinrock et al., 1996); (2) top of the basement in TAG-4 (Hole 957M) at 3687 mbsl; (3) line showing the shallowest level at which altered basalt clasts were recovered within the mound; (4) top of the basement in TAG-2 (Hole 957B) at 3672 mbsl; (5) basalt sample recovered post-drilling from southeast edge of the mound at 3650 mbsl (Kleinrock, in lit.); (6) regional depths of the seafloor south and east of the mound at 3660 to 3670 mbsl, respectively (Kleinrock et al., 1996); (7) basalt with chloritized halos sampled from northeast edge of the mound at 3675 mbsl (Masuda et al., 1995); (8) basalt sample recovered post-drilling from northeast edge of the mound at 3677 mbsl (Kleinrock, in lit., 1996).

Several of these samples also exhibit a < 1-mm-thick, outer, red halo. A centimeter-sized fragment of massive hydrothermal quartz, which may be interpillow material, was also recovered from this interval, along with two chloritized basalt fragments, one of which contains a millimeter-wide vein of quartz + sulfides.

Between 42.5 and 24.5 mbsf, numerous fragments of pyritized, silicified, and paragonitized wallrock breccia were recovered in 22 core pieces. They are interstratified with 15 pieces of “pyrite silica breccias” and “massive granular pyrite aggregates” and two pieces of either gray or red chert pieces. The pieces of hydrothermally altered wallrock are more numerous than the hydrothermal precipitates (22 vs. 17). The clasts of hydrothermally altered basaltic material in Hole 957M are more rounded than elsewhere beneath the TAG mound, and are cemented by common pyrite and lesser quartz than elsewhere, suggesting that this hole penetrated a former rubble pile (Humphris, Herzig, Miller, et al., 1996).

The dominant rock types of the uppermost 24.5 m of the section are interstratified massive but porous pyrite ± marcasite aggregates and pyrite ± marcasite silica breccias, both with abundant colloform, banded textures. Minor chalcopyrite and traces of sphalerite are often present. Chert and Fe-oxyhydroxide and oxide pieces are intermixed with the sulfides. The top 70 cm of the hole consists of drill cuttings composed of reddish brown or orange Fe-oxyhydroxides with minor pyrite and silica. The shallowest hydrothermally altered basalt clast was observed in Sample 957M-1R-2 (Piece, 19–23 cm), which was recovered only 74 cm from the top of the hole. Unlike all other holes drilled on the mound, no anhydrite was found in Hole 957M.

#### Holes 957P (TAG-5 area) and 957H (TAG-2 area)

Silicified wallrock breccias similar to those from the TAG-1 area occur from about 25 mbsf to the bottom of the hole at 54.5 mbsf in Hole 957H, in the TAG-2 area on the southeast side of the mound. As in the TAG-1 area, these rocks are overlain by pyrite-silica breccia, pyrite-anhydrite breccias, and then pyritic breccias plus massive pyrite near the top of the mound. Anhydrite veins are common through-

out. The presence of stockwork rocks (silicified wallrock breccias) in this hole and their absence in nearby Hole 957B defines the outer edge of the stockwork beneath this portion of the mound.

Generally similar silicified wallrock breccias also occur in Hole 957P, in the TAG-5 area on the northern side of the mound. Here these rocks occur from 35 mbsf to the bottom of the hole at 59.4 mbsf. Late anhydrite veins are common, and the rocks are cemented by massive pyrite, cut by common centimeter-thick pyrite veins, and rock fragments are partly replaced by pyrite along their margins. This portion of the stockwork is thus more sulfide rich than elsewhere beneath the mound. These rocks are overlain by pyrite-silica breccias, pyrite-anhydrite breccias, and then pyritic breccias and massive pyrite near the surface of the mound.

#### Alteration Lithostratigraphy in the Central Part of the Mound

##### Holes 957C to G and L (TAG-1 area)

Six holes were drilled near the Black Smoker Complex, at the top of the upper terrace, at a water depth of 3645 m, i.e., in TAG-1 area (Holes 957C to 957G and 957L). Holes 957E and 957C are located about 10 m southeast of the central Black Smoker Complex, and were started from the same water depth of 3645 m. These holes compose a reference section for the lithostratigraphy of the active mound and the stockwork near the upflow zone because they are the deepest holes drilled during Leg 158 (i.e., from 10 to 125.70 mbsf). However, the recovery in Hole 957E was a low 4.3% and, therefore, our observations are supplemented by those from the Hole 957C section, which was drilled from 10 to 49 mbsf with a recovery of 44%. Shipboard descriptions of cores from Holes 957F (from the surface to about 8 mbsf, with 10.5% recovery) and 957G (from 12 to 22 mbsf, with 8.5% recovery) were used to reconstruct the upper lithostratigraphy.

Starting from the deepest core samples collected during Leg 158, Section 957E-18R-1 (Pieces 1-9), the deepest recovered part of the stockwork beneath the central discharge conduit consists of at least 15 m of chloritized basalt fragments and breccias, as well as basalt to-

tally replaced by paragonite + quartz + pyrite. These rocks are cut by thin pyrite and quartz veins and are interstratified with rare occurrences of pyrite-silica breccias. The latter could represent fragments of thicker pyrite-quartz veins because the size of the five samples encountered ranges from 1 to 6 cm across. Almost all of the rock fragments recovered exhibit mm-thick anhydrite coatings on portions of their outer surfaces. These coatings are interpreted to be the remains of late anhydrite veins, along which the rocks fractured during coring. Their pre-drilling widths were at least 1 mm to 2 mm.

The chloritized basalt in the deepest 15 m of the core is progressively replaced by paragonite + quartz + pyrite in rims around chloritized basalt clasts and along veins crossing the latter (see next section "Petrographic Descriptions"). The paragonitized rocks are called "silicified wallrock breccia" in the Leg 158 *Initial Reports* volume. Chlorite disappears as a major secondary mineral of the stockwork above 111 mbsf. Above 101 mbsf, the same paragonite + quartz + pyrite assemblage occurs, but the rocks are more intensely silicified. As a consequence, the rock type forming the stockwork changes from a mixture of completely chloritized rocks plus rocks replaced by paragonite + quartz + pyrite, to only the totally paragonitized + pyritized + silicified basalt above 111 mbsf. The latter rock type is present as silicified wallrock breccias and hydrothermally altered clasts ranging from 0.1 mm to 70 mm in size. Portions of the outer surfaces of most of the rock fragments recovered exhibit millimeter-thick anhydrite coatings, which are the remains of late anhydrite veins. The pre-drilling widths of these veins were at least 1–2 mm. The silicified wallrock breccias and hydrothermally altered clasts are intermixed within pyrite silica breccias and anhydrite veins below about 25 to 35 mbsf. Anhydrite veins in Hole 957C (down to 50 mbsf) range from a few millimeters up to 45 cm in thickness. In contrast, anhydrite veins and coatings in Hole 957E over the interval where these cores overlap (40–50 mbsf) are <1–2 mm thick. Core recovery in Hole 957C was an order of magnitude greater than in Hole 957E (45% vs. 4.3%), suggesting that many of the thin anhydrite coatings (veins) on rock fragments deeper in Hole 957E correspond to veins of unknown thickness, but probably much thicker than the observed 1–2 mm thick. Even though poor core recovery could be a result of a number of factors, we think that the abundance of anhydrite veins represents, in the context of the central part of the TAG mound, the weakest mechanical lithology feasible to be lost during drilling. Holes 957E and 957C were drilled only a few meters apart in otherwise very similar lithologies.

The hydrothermally altered clasts within pyrite silica breccias generally decrease in amount upward from 92.22 mbsf to 49 mbsf. No hydrothermally altered basalt clasts were encountered at shallower depths in Hole 957E (to 31.50 mbsf, the shallowest core at the top of Hole 957E). The shallowest hydrothermally altered basalt clasts were observed at 16.55 mbsf in Hole 957G in a "massive granular pyrite breccia" (i.e., in Sample 957G-2N-1 [Piece 9, 2–5 cm]) and at 19.50 mbsf in Hole 957C (a 1–2-cm buff-colored basalt fragment in a "nodular siliceous pyrite-anhydrite breccia" of Sample 957C-7N-1 [Piece 6G, 58–68 cm]). Several other basalt clasts were found at 21.35 and 21.69 mbsf in Samples 957G-3N-1, 34.5–65 cm (Pieces 4A–D) and 957G-3N-1, 68–77.5 cm (Piece 6).

### Other Basalt Samples from the TAG Mound

Submersible observations have three times reported the occurrence of basaltic rocks on and around the TAG mound. Lisitsyn et al. (1989) report that "the floor around the hydrothermal mound is shattered basaltic basement..." and "on the upper slope, two fragments of basalt tubes with sectoral parting were found." Reasonably, one ought to question the "greenstone-altered basalts" identification mentioned by Lisitsyn et al. (1989) because nontronite, which cements the basalt fragments along with quartz or opal, birnessite and iron oxides, or sulfides, is, according to these authors, the only clay mineral

identified by X-ray diffraction. If nontronite is green enough to lead to the name "greenstone," it is probably a low-temperature hydrothermal phase unrelated to sulfide mineralization.

Post-drilling dives reported (see Fig. 3) basalt "from the (SE) steep flank of the lower terrace a couple of meters below the lip of that terrace and perhaps 10 m to 20 m above the surrounding seafloor...The depth from the ALVIN pressure gauge was 3650 m. A second sample was collected from the northeast edge of the mound (also on the slope)...at a depth of 3677 m." (Kleinrock, in lit., 1996). However, no description is given of any basaltic rock collected during the two above mentioned submersible surveys. It is remarkable that no other basalt occurrences have been reported during the numerous U.S., Japanese, and French submersible dives on the TAG mound.

On the other hand, a 10 cm long basalt fragment was collected (see location on Fig. 3) during a NANKAI submersible dive on the NE foot of the TAG mound, at 3675 m water depth (Masuda et al., 1995). This sample displayed a 2.5-cm-thick chloritized rim (without primary plagioclase) around a smectite-bearing core (containing primary plagioclase) and is quite similar to samples cored from the bottom of Hole 957M. The depth at which this sample was collected at the northeast foot of the mound is about the same (within depth measurement error) as that where the top of the chloritized basement was encountered in Hole 957B in the southeast part of the mound (see Fig. 3). This depth also corresponds to that of the regional seafloor surface according to Kleinrock et al. (1996). Whether chloritized basaltic rock fragments or any other type of hydrothermally altered basement material actually occur on the mound and around it is significant. For instance Lisitsyn and his co-authors (1989) deduced from the presence of basaltic rock fragments on top of the active TAG mound (as well as "fragments of greenstone-altered basalt... cemented with ore material" from the inactive *Mir* mound) that these sulfide mounds were built up on basaltic debris and hydrothermally altered basalt. Their figures 2 and 4 are explicit about this hypothesis.

### Summary of Alteration Lithostratigraphy

In summary (see Fig. 3), the stockwork beneath the TAG mound is zoned vertically and laterally and is less than about 100 m wide. The deepest portion of basement drilled beneath the central portion of the TAG mound (i.e., in Hole 957E at 125.7 to 111 mbsf) consists of basalts totally replaced by an assemblage of chlorite + pyrite + quartz, which is in turn partly to totally replaced by paragonite + quartz + pyrite in this depth interval. These rocks give way to rocks totally replaced by the paragonite + quartz + pyrite assemblage up to 101 mbsf, above which similar, though more silicified, rocks occur to shallower depths. Similar paragonite + quartz + pyrite assemblages totally replace basement in Holes 957H, 957P, and 957M on the southeast, north, and west sides of the mound, respectively, although rocks in Hole 957P are more pyritized, and the recovery from Hole 957M on the west side of the mound probably represents a rubble pile. Anhydrite veins are common throughout all of the sections, with the exception of TAG-4.

Isolated, centimeter-sized, clasts of basalt also occur along with pyrite + quartz clasts forming the various types of pyrite-silica breccias. The size and abundance of these hydrothermally altered basalt clasts decrease irregularly upward. The uppermost such clasts were found at only 0.74 mbsf in Hole 957M (west margin), at 9.75 mbsf in Hole 957N (40 m south of mound center), at 16 mbsf in Hole 957C and at 20 mbsf in Hole 957G (both at mound center), and at 17 mbsf in Hole 957O and 35 mbsf in Hole 957P (both at north margin). The uppermost clast found in Hole 957H of TAG-2 southeast distal area occurred at 34 mbsf, which is relatively deep, but the lack of documented basalt clasts higher in this section does not preclude their presence because of the low core recovery.

Slightly altered basalt with chloritization halos was encountered beneath the mound margins at a much shallower depth than near the present discharge zone: 42 mbsf or 3695 mbsl under the northwest distal part of the mound of TAG-4 where the regional seafloor depth is 3688 m, according to the detailed bathymetry map of Kleinrock et al. (1996).

## PETROGRAPHIC DESCRIPTIONS

The most common rock type recovered from within the active hydrothermal TAG mound during ODP Leg 158 are various types of breccias made up of several generations of sulfides (mainly pyrite), quartz, and anhydrite in variable proportions. These three hydrothermal minerals occur as clasts, as cement, or as veins.

The variably altered basaltic rocks and clasts recovered by drilling of the basement beneath and within the mound are fragments of pillow basalts, interpillow breccias or hyaloclastites with holohyaline, variolitic, and subvariolitic textures are generally observed. These fragments are either clasts ranging in size from a few millimeters across (i.e., they could only be identified in thin section or with a hand lens) to a few centimeter in diameter, to veined blocks as large as the core diameter (i.e., about 6 cm) and larger.

### Basement Beneath the Mound Margins

Basement beneath the mound margins (Holes 957B on the southeast, and 957M on the west) contain the least altered rocks, as well as chloritized rocks that differ from those in the deep chloritic stockwork zone. The basal part of Hole 957B contains slightly altered, smectite-bearing dark gray basalts that exhibit centimeter-sized, variably altered red halos (see Pl. 1, Fig. 1). Chloritized rocks are also present. In the lower portion of Hole 957M, lightly altered, smectite-bearing dark gray basalts bordered by centimeter-wide chloritized alteration halos with or without an outer millimeters-wide red band were recovered. Specific samples of these rocks are described in detail below.

#### Hole 957B

Sample 158-957B-4R-1 (Piece 6) 48–49 cm, is a 4.5-cm-long fragment of subvariolitic aphyric basalt. It displays three concentric alternately light and dark reddish brown bands, about 2 mm thick, around a reddish brown to bluish gray mottled core (see Pl. 1, Fig. 2). The grayish zones in the core correspond to unstained basalt matrix, whereas the reddish ones are stained by Fe-oxyhydroxides. Euhedral olivine microphenocrysts and skeletal crystals are intensively replaced by smectite (with or without talc, see “Phyllosilicate Mineralogy” section) with little Fe-oxyhydroxides. Only a few rare 80- $\mu$ m-diameter olivine relics are left at the center of the larger olivine crystals (see Pl. 1, Fig. 3). Plagioclase microlites appear to be unaltered in the sample core, whereas they are almost completely replaced by colorless smectite in the sample’s outer reddish rims. Vesicles ranging from 70 to 300  $\mu$ m in diameter are filled with zoned, fibroradial smectite. A few miarolitic voids are filled with yellow smectite stained by Fe-oxyhydroxides. A 0.4-mm-thick hematite + lepidocrocite vein crosses one corner of the sample (see Pl. 1, Fig. 4). The vein displays diffuse selvages because the Fe-oxyhydroxides selectively replaced the basaltic matrix between the plagioclase microlites. Several twisted veinlets (4 to 100  $\mu$ m thick) of probably the same Fe-hydroxides are observed. Disseminated pyrite is common and chalcopyrite rare. Both sulfides occur as granules, 1 to 20  $\mu$ m in diameter, in interstitial areas, along fractures, and on vesicle walls. Pyrite crystals, 50 to 80  $\mu$ m in diameter, with minor chalcopyrite, covellite and bornite are associated with these smectite veinlets in the bluish gray portions of the sample core. In contrast, the red halos of at least some

other samples are totally recrystallized to chlorite (see Pl. 1, Fig. 1; Sample 158-957B-4R-1 [Piece 2, 17–24]).

Sample 158-957B-4R-1 (Piece 3, 30–38) between the samples just described, is a completely altered pillow rim breccia made up of millimeter- to centimeter-sized angular to subangular glass and microcrystalline basalt clasts loosely cemented by a soft chlorite + hematite + quartz mud (see Pl. 1, Fig. 1). The alteration patterns displayed by the shards are extremely varied and complex: convoluted color zoning ranges from dark reddish brown to almost colorless, and Liesegang banding is frequently observed in the altered glass. The alteration predated the breaking up of the shards because the alteration patterns are not concentric with the shard outlines but intersect them. X-ray diffraction of several bulk rock samples and <2- $\mu$ m fractions indicate that chlorite, quartz, and hematite are the only minerals present in this sample. Chlorite with and without hematite staining replaces the basaltic material. Chlorite frequently occurs as pseudomorphs after olivine microphenocrysts and skeletal olivine crystals and probably after plagioclase microlites, but the secondary mineral replacing plagioclase could not be optically identified. Relict varioles and vesicle infillings are now represented by fibroradial chlorite aggregates. A few glass shards exhibit “parquetry” patterns resulting from adjacent patches about 500  $\mu$ m long on edge, which are made up of subparallel, 40- $\mu$ m-long chlorite fibers. The breccia cement consists of 8- to 150- $\mu$ m-diameter anhedral quartz grains with common wavy extinction, finely fibrous chlorite, and dark reddish brown anhedral hematite. Locally, larger quartz grains tend to gather and form quartzitic granules, a few millimeters in size. Hematite is also locally present as an interstitial coating of the quartz granules.

#### Hole 957M

Green chloritic alteration zones with disseminated pyrite are common but not ubiquitous among the 44 pieces of basalt recovered in Cores 158-957M 9R-1, 10R-1, and 10R-2, from the basement beneath the western margin of the mound. These samples, up to 6.7 cm in length, are the largest basalt fragments recovered during Leg 158. The green halos are concentric with the piece outlines and with respect to sometimes present inner, almost black bands, up to 5 mm thick, and surround the dark gray cores of less altered basalt (see Pl. 2, Fig. 1 of Sample 158-957M-9R-1 (Piece 6, 31–37 cm), and Pl. 2, Fig. 2 of Sample 158-957M-10R-1 (Piece 21, 140–146 cm)). Green halos are more common in samples from Cores 158-957M-10R-1 and 10R-2 than in those from Core 158-957M-9R-1 (see Pl. 2, Fig. 3). According to the Leg 158 *Initial Reports* (Humphris, Herzig, Miller, et al., 1996), the thickness of the green halos ranges from 0.5 to 50 mm, but the actual thickness is difficult to assess because outer halos were partly removed by the coring process.

The inner basalt cores with subvariolitic textures have been weakly altered at low temperature so that only their olivine microphenocrysts and skeletal crystals are generally but to a very slight extent replaced by smectites with traces of “iddingsite,” i.e., mixtures of Fe-oxyhydroxides and smectite, along their outlines and cracks (see Pl. 2, Fig. 4). The plagioclase microlites, plumose clinopyroxenes and Cr-spinels are essentially unaltered. Vesicles and miarolitic voids are filled with smectite and rare iddingsite in the less altered, dark gray inner portions of basalt fragments.

In the green halos, olivine is commonly almost completely replaced by chlorite and mixed-layer smectite-chlorite, whereas the vesicles and miarolitic voids are filled with these minerals (see Pl. 2, Fig. 5). The basaltic groundmass is lighter colored in the green halos than in the less altered cores probably as a result of the pervasive replacement of interstitial material by chloritic phyllosilicates. Thin, <0.1-mm-thick, chlorite veins and apparently discontinuous pyrite veins are present.

Fe-oxyhydroxides are locally observed associated with the chlorite or smectite replacing the olivine and filling vesicles and miarolitic

tic voids in the green halos and associated rocks. Samples 158-957M-10R-1 (Piece 6, 33–35 cm, and Piece 9, 60–62 cm) exhibit up to 2-mm-thick, brown red halos in which olivine is mainly replaced by smectite and iddingsite with few relics left. The plagioclase microclites are stained by orange-brown Fe-oxyhydroxides, and the vesicles lined with a Fe-oxyhydroxide layer up to 25  $\mu\text{m}$  thick; veinlets of pale yellowish-tan fibrous smectite 50- to 100- $\mu\text{m}$ -thick cross the red halos.

In a few samples, (Samples 158-957M-10R-1 [Piece 9, 60–68 cm], and [Piece 10, 69–75 cm]), the chloritic, pyrite-bearing halos grade outward into a several millimeter-thick reddish brown band in which the disseminated pyrite is replaced by Fe-oxyhydroxides that may correspond to a later (maybe present-day) oxidation of the sulfide.

Sample 158-957M-10R-2 (Piece 7, 31–32 cm) is a pervasively chloritized pillow lava rim with a coalesced variole texture corresponding to Kirkpatrick's (1978) N<sup>4</sup> zone (see Pl. 2, Fig. 1). The hand specimen displays a green color and clearly shows 2-mm-thick, double, green halos (i.e., lighter toward the vein and darker toward the host rock) bordering both selvages of a 2.5- to 5-mm-thick quartz + pyrite vein. The old glassy rim and adjacent submicroscopic basalt matrix is probably completely replaced by brownish tan chlorite, whereas the glomerophytic olivine microphenocrysts are replaced by quartz + pyrite + pale green chlorite. Vesicles up to 0.2 mm in diameter are filled with brown fibroradial chlorite. Pyrite crystals are disseminated in the host-rock on both sides of the vein selvages with a decreasing average grain size away from the selvage. Near the vein, the euhedral pyrite crystals are up to 0.1 mm on edge with a few micrometer-thick quartz corona whereas they decrease down to about 0.008 mm in diameter 2 to 3 mm farther inside the host-rock. The main vein corresponds to multiple stage fillings of an open crack by several generations of quartz with disseminated pyrite, frequently leaving chloritized rock screens between successive quartz layers. The anhedral quartz crystals are generally "dirty," range up to 0.7 mm in length, and generally exhibit wavy extinction. There are a few interstitial brownish phyllosilicate flakes among the quartz crystals. Several quartz or quartz + euhedral pyrite veinlets, ranging from 0.008 to 0.1 mm in thickness, criss-cross the host-rock and the main quartz + pyrite vein. A pale green chlorite discontinuously lines the walls of one such vein, whereas euhedral pyrite occupies its center.

The "crystalline calcite" and "minor calcite" reported in the Leg 158 *Initial Report* core descriptions (Humphris, Herzig, Miller, et al., 1996) as lining vesicles in pieces from Cores 158-957-9R-1 and 10R-1 (see Humphris, Herzig, Miller, et al., 1996, p. 309–310) have not been observed in any of the study thin-sections, and no carbonate was identified in any of the samples from Leg 158 that we have analyzed.

## Deep Chloritic Stockwork

### Chloritized Basalts

Sample 158-957E 18R-1 (Piece 1, 0–8 cm) was collected at 120.70 mbsf, and represents one end-member type of hydrothermal alteration (chloritization) characteristic of the deepest drilled portion beneath the central part of the mound (111 to 125.7 mbsf). The sample is a relatively large (7 cm across) fragment of greenstone (see Pl. 3, Fig. 1) corresponding to a chloritized intergranular basalt containing chlorite, quartz and pyrite, in decreasing order of abundance (see "Phyllosilicate Mineralogy" section). It is intersected by chlorite + quartz + pyrite veins ranging from 0.05 to 1 mm in thickness; a 1-cm-thick anhydrite + pyrite vein runs along one side of the sample (see Pl. 3, Fig. 1). Chlorites of variable composition (see "Phyllosilicate Mineralogy" section) and anhedral quartz replace primary plagioclase phenocrysts, microphenocrysts and microlites. Primary glomerophytic olivine aggregates are replaced by chlorite, anhedral quartz and subhedral sulfides (mainly pyrite with minor chalcopyrite) (see Pl. 3, Fig. 2). Cr-spinel is the only primary mineral that has not been

completely replaced by hydrothermal phases. The rims of the largest Cr-spinel crystals, ranging from 0.1 to 0.3 mm in diameter, are altered and smaller crystals are almost totally replaced by an unidentified phase. Vesicles and miarolitic voids, ranging from 0.15 to 0.75 mm in diameter are filled with concentrically zoned fibroradial chlorite with occasional anhedral quartz at the center.

Four types of veins were observed:

1. One, with matching parallel selvages, starts as a 0.05- to 0.06-mm-thick, double fibrous chlorite-filled vein. As it increases up to 0.016 to 0.025 mm in thickness, anhedral quartz crystals and then subhedral pyrite crystals successively appear at the center of the vein leaving two chlorite selvages. Finally, where it is the thickest (about 0.75 mm across), the vein does not contain any chlorite and it is made up of quartz selvages with subhedral pyrite crystals at its center (see Pl. 3, Fig. 3). "Dirty" anhedral quartz crystals are often seen at the center of the vein (see Pl. 3, Fig. 3). Such quartz crystals contain parallel alignments of tiny brown particles (see "Phyllosilicate Mineralogy" section). Pyrite commonly overgrows the vein walls and replaces the adjacent chloritized host-rock. This first vein type clearly indicates that chlorite formed first in an open fissure, followed by quartz, and finally pyrite.
2. Later veins are composed mostly of quartz alone, are very irregular in shape, and variable in thickness, ranging from 0.3 to 1 mm across; hence, they do not display matching selvages and did not form by open crack fillings but by replacement of the host-rock. Rarely, they locally contain few small anhedral pyrite crystals or chlorite aggregates.
3. Another type of later vein is formed by pyrite alone. These appear in the two-dimensional thin section surface as apparently discontinuous alignments of 0.03 to 0.15 mm subhedral pyrite crystals. This type of vein results from the total replacement of the chloritized host-rock.
4. Anhydrite and euhedral pyrite are commonly observed coating one side of samples (see Pl. 3, Fig. 1). These minerals probably form one of the latest veins but could also be part of the matrix in a coarse greenstone breccia.

### Chloritized Basalts Partly Replaced by Paragonite + Quartz + Pyrite

Sample 158-957E 18R-1 (Piece 4, 20–24) was collected at 120.9 mbsf, and illustrates the further reaction of chloritized rocks and their replacement by paragonite + quartz + pyrite in the deepest rocks drilled (111 to 125.7 mbsf). The sample consists of a 1.5-cm clast of hydrothermally altered basalt rimmed by a 1-cm-thick breccia of altered glass shards cemented by quartz (see Pl. 3, Fig. 5).

The altered basalt clast consists of 5-mm-sized islands of green chloritized intergranular basalt, rimmed by 2- to 3-mm buff-colored halos where the rock is completely replaced by paragonite + quartz + pyrite. In the chloritized portion of the basalt, the microlitic groundmass is replaced by chlorite and disseminated pyrite; plagioclase microlites and microphenocrysts are replaced by polycrystalline quartz and traces of chlorite; olivine microphenocrysts are replaced by quartz, or chlorite with minor quartz, and pyrite. In the buff-colored halos along the margins of the fragment and along a 0.75-mm-thick quartz + pyrite vein, alteration is similar to that in the chloritized portion, but chlorite is replaced by paragonite. The subvolcanic groundmass is replaced by paragonite and disseminated pyrite; plagioclase microlites and microphenocrysts are replaced by quartz and traces of paragonite; olivine microphenocrysts are replaced by quartz, or paragonite with minor quartz, and pyrite. A pair of 0.09-mm Cr-spinel crystals with rounded outlines are the only primary minerals observed in the thin section of this sample. The Cr-spinel is present near the center of a 1.2-mm diameter aggregate made up of

six anhedral quartz crystals, several subhedral pyrite crystals, and white mica flakes. This quartz + pyrite + mica aggregate may be replacing an olivine + Cr-spinel primary glomerophytic aggregate.

The green chloritized portion of the basalt fragment is cut by a 0.24-mm-thick, pale green chlorite vein with clear, subparallel selvages that contains rare euhedral pyrite crystals. This earliest vein is intersected by a 0.75-mm-thick quartz + pyrite vein with poorly defined selvages. Pyrite is located mainly at the center of the vein. In a 1-mm-wide zone along both sides of the quartz + pyrite vein, the host rock is totally replaced by paragonite + quartz + pyrite, and the chlorite vein is replaced by paragonite (see Fig. 3, "Phyllosilicate Mineralogy" section). The same chlorite vein is intersected and displaced by a 0.03-mm quartz-thick vein. There are numerous bifurcating, anastomosing quartz veins, 0.04 to 0.12 mm thick, with a few pyrite crystals.

In the breccia surrounding and cementing the basalt clast, altered glass shards, ranging from 0.06 to 0.6 mm in diameter, are angular and commonly display concentric alteration zoning. The glass is replaced by a green brown chlorite, itself locally replaced by paragonite, quartz, and pyrite in variable proportions.

In the matrix, the quartz + pyrite veins are difficult to distinguish from the quartz + pyrite matrix of the breccia. Quartz crystals commonly appear "dirty" because of numerous submicroscopic inclusions, and they range from chalcedony-size grains (i.e., ranging from a few micrometers to several tens of micrometers) to 0.5-mm-long elongated crystals. The latter commonly contain the tiny inclusions only in their center.

Sample 158-957E 18R-1 (Piece 5, 30–31 cm) is a hydrothermally altered breccia composed of halohyaline to fine-grained intergranular clasts cemented by generally dirty quartz and pyrite crystals ranging from < 10  $\mu\text{m}$  to 0.25 mm in diameter.

The old glassy clasts are often pseudomorphed by greenish to almost colorless fibrous chlorite (with or without paragonite) often forming large (0.15 mm long and 0.02 mm thick) tufts, whereas the clasts with an intergranular texture are generally replaced by dirty quartz, pyrite, chlorite, and paragonite mixtures (see Pl. 3, Fig. 6). Olivine microphe-nocrysts totally replaced by green chlorite, and vesicles filled with fibrous chlorite with locally anhedral quartz crystals at the center were observed in old glassy clasts. In the clasts with relict intergranular texture, the plagioclase microlites are totally replaced by quartz, whereas the fibrous chlorite fillings of the vesicles are partly replaced by paragonite. Irregularly shaped veins ranging from 0.15 to 15 mm in thickness criss-cross the breccia and often clearly cut across the clasts. The veins are formed by anhedral, often "dirty," quartz and elongated aggregates of euhedral pyrite crystals that occupy the center of the veins or by pyrite alone. Selvages of the veins are generally difficult to define because the vein minerals are the same as those forming the breccia matrix. It is only when veins cross a clast with holohyaline or fine-grained intersertal texture that the vein selvages are visible. Minor anhydrite can also be present at the center of the thickest veins.

### Main Paragonite + Quartz + Pyrite Stockwork

Above 111 mbsf, all basalt clasts in the TAG-1 area are completely replaced by paragonite + quartz + pyrite in variable proportions (see Pl. 4, Figs. 1 to 4). Late anhydrite veins are common throughout, and the intensity of silicification increases above 101 mbsf. A similar uphole alteration pattern was observed in drilled sections from TAG-1, 2 and 5. The following petrographic description is a composite of microscope observations on a collection of about 150 thin sections.

This series of thin sections allowed us to reconstruct the progressive evolution of basaltic clasts of the stockwork near the active upflow zone of hydrothermal solutions beneath the central part of the mound. The evolution is observed along a 70-m-thick section through the basement.

The inner parts of the largest clasts, which in the least altered samples are about 2–3 cm across, clearly exhibit characteristic quenching features of basaltic lavas emplaced during subaqueous eruptions. The textures range from intergranular with skeletal lath-shaped plagioclase microlites and olivine microphe-nocrysts, and dendritic clinopyroxene (Zone 6 texture of pillow lavas according to Kirkpatrick [1978]), to "bow-tie" spherulites to coalesced plagioclase spherulites and olivine dendrites with poorly defined or undefined spherulite boundaries (Zones 5 and 4, respectively of Kirkpatrick's [1978] subvariolic textures). The more glassy Zones 1 to 3 (Kirkpatrick, 1978) are rarely observed, probably because holohyaline clasts with well defined, isolated spherulites (i.e., varioles), are either less abundant or they have been totally replaced by quartz + pyrite + mica mixtures, and, therefore, their igneous texture has been obliterated. A 5 mm or a 10 mm thick glassy pillow rim corresponding to Kirkpatrick's (1978) zones 1 to 3 only represents 5.9 or 7.7% by volume of a 50 cm in diameter pillow lava. Vesicles ranging from 0.1 to 2.5 mm in diameter are filled by the same types of secondary minerals as those that replace the host basaltic clasts. Very often fibroradial paragonite with rare chlorite lines the walls of the vesicles, whereas small anhedral to subhedral quartz and/or pyrite crystals are found near the center. More rarely, the vesicles are filled by paragonite alone (this is often the case in the least altered parts of the clasts, see Pl. 5, Fig. 1), quartz alone or quartz near the walls and pyrite at center. Segregation vesicles (Bideau and Hekinian, 1984), ~0.25 mm in diameter, with the characteristic frozen meniscus of solidified residual magmatic melt are filled by paragonite.

As a result of intense silicification and pyritization, the primary, magmatic textures of the basalt clasts progressively disappear. Quartz + pyrite + paragonite pseudomorphs after olivine microphe-nocrysts are rarely observed in an almost completely obliterated subvariolic groundmass (see Pl. 5, Fig. 2). The complete evolution can be clearly observed when one compares the various parts within a single clast in one thin-section, moving from the inner part of the clast to its edges (see Pl. 5, Figs. 3 to 8). The inner part of clasts contain scattered euhedral to subhedral pyrite crystals, ranging from 15 to 300  $\mu\text{m}$  but most about 25  $\mu\text{m}$  on edge. They are generally surrounded by polycrystalline anhedral quartz coronas about 10 to 50  $\mu\text{m}$  thick, which almost completely surround the pyrite crystals (see Pl. 5, Fig. 3). Moving toward the clast edges, or near a quartz + pyrite vein crossing the clast, pyrite crystals and their quartz coronas become progressively more abundant, coalesce and finally merge, forming discontinuous zigzagging festoons of quartz and pyrite (see Pl. 5, Fig. 4). As a result, the basalt clasts appear to be concentrically framed by irregularly shaped quartz + pyrite veins whose size and abundance increase from the clast cores to their edges (see Pl. 5, Fig. 5 and 6). These festoons do not differ in composition nor in shape from the thicker quartz + pyrite veins that separate the various clasts or clast fragments in a single sample. The overall picture is of "expanding" clasts with centripetally increasing quartz and pyrite. Both in the inter- and intraclast veins, pyrite is most often localized near the center with respect to quartz, which forms the vein selvages (see Pl. 5, Figs. 4–6).

The most resistant primary feature of the basaltic clasts is their "bow-tie" microlitic texture which is often observed, though sometimes very faintly, within "dirty" or "cloudy" quartz crystals of the breccia matrix or of the quartz + pyrite veins (see Pl. 6, Fig. 1). Much quartz appears "dirty" because it contains subparallel alignments of abundant, submicroscopic to micron-sized, brownish inclusions which cut across adjacent crystal boundaries and sometimes extend across 3 or 4 contiguous crystals (see Pl. 6, Figs. 2–4). These features are very similar in dimension and geometry to the primary "bow-tie" microlitic texture of the primary subvariolic basalts that are formed by tufts of skeletal plagioclase microlites separated from each others by dark Fe-Mg rich mesostasis. Quite often the "dirty" quartz crystals are located at or near the center of the veins as if they correspond to

former rock screens (see Pl. 3, Fig. 3 in the case of a chloritized basalt). Large, up to 0.5-mm-long, elongated quartz crystals are often dirty in their central part whereas their two ends are limpid because they are inclusion free.

As inferred from electron microprobe analyses, the inclusions making the quartz crystals appear “dirty” consist essentially of paragonite flakes, more rarely chlorite, and even more rarely unidentified Ti-rich phases (anatase or rutile?), which are probably oxides because they did not contain any major element but Ti. Fluid inclusions are present as well. In Sample 158-957P-8R-1, 5–7 cm, “dirty” quartz contained a few spots of an unidentified Cr-rich phase near Cr-rich paragonite, the chemical composition of which is discussed in the “Phyllosilicate Mineralogy” section. It is uncertain whether these represent the incorporation into paragonite of Cr derived from the breakdown of primary Cr-spinel, or contamination by cryptocrystalline inclusions of a Cr-phase within the paragonite flakes that are enclosed in the “dirty quartz.”

Four types of veins criss-cross the basalt clasts:

1. The most abundant veins are irregularly shaped (without parallel selvages) quartz + pyrite veins (see Pl. 7, Fig. 1). Several generations of these veins intersect each other and cut rare earlier chlorite veins. The quartz + pyrite veins mostly cut orthogonally across the basaltic clasts, but in some cases they are difficult to distinguish from the quartz + pyrite cement of the breccias (see Pl. 7, Fig. 2). The quartz + pyrite veins vary from about 0.5 mm to 4 mm in thickness but their actual thickness is generally hard to measure because of the lack of clear-cut selvages, in which cases the veins blend with the breccia cement. Within clasts, the vein thickness ranges from 0.15 mm to 0.8 mm. Aggregates of subhedral pyrite crystals generally occupy the central part of the quartz + pyrite veins, and the largest pyrite crystals sometimes overgrow the vein width and protrude into the adjacent host-material, consisting of either clast or cement. The quartz crystals of the quartz + pyrite veins are anhedral to subhedral and often appear “dirty.”
2. Paragonite is a common but minor vein constituent throughout these rocks. It occurs as tens to hundreds of micrometer-sized, colorless patches along the selvages of the quartz + pyrite veins, either interstitial to these minerals (see Pl. 7, Fig. 3) or making up a significant proportion of the vein. Paragonite is also common as cloudy, brownish, fibrous, material interstitial to pyrite (see Pl. 7, Fig. 4).
3. Chlorite is present in trace amounts in veins throughout the paragonite + quartz + pyrite stockwork. It occurs as small (about 10  $\mu\text{m}$  in diameter) isolated spherules or larger aggregates (tens to hundreds of micrometers) interstitial to quartz and pyrite in veins.
4. Anhydrite veins are the second most abundant type of vein, and anhydrite is also common as millimeter-thick coatings on broken faces of hand specimens. Anhydrite is a late phase in vuggy quartz + pyrite veins, and forms with these minerals rare veins up to 0.15 mm thick.

### PHYLLOSILICATE MINERALOGY

Chlorite and/or paragonite are the most frequently observed clay minerals in the various samples of hydrothermally altered basalts from the cores of the TAG mound. They form flakes ranging from a few micrometers to 75  $\mu\text{m}$  in length.

These two clay minerals occur as optically distinct phases. Chlorite is colorless, brownish, or light green in color, has low birefringence quite often with anomalous colors, and displays parallel extinction, whereas paragonite is colorless to tan, has middle-high birefringence and parallel extinction. The latter optical properties exactly

correspond to those of white micas (i.e., sericite or muscovite), and the white mica structure was confirmed by X-ray diffractions, but all the electron microprobe analyses clearly indicate a Na-rich composition (see Fig. 4).

### Paragonite

Paragonite is a dioctahedral sodium mica,  $\text{NaAl}_2\text{Si}_3\text{AlO}_{10}(\text{OH})_2$ , having complete solid solution with muscovite at temperatures  $>550^\circ\text{C}$ , but with significantly decreasing solution at lower temperatures (Guidotti et al., 1994). Electron microprobe analyses and X-ray diffraction of TAG “paragonites,” however, reveal that these are mixtures of paragonite and dioctahedral smectite. Interlayer cations of TAG paragonites are predominantly Na (see Fig. 4), but total interlayer cation contents are variable and lower than pure paragonite (Fig. 5), consistent with the presence of differing amounts of smectite layers. TAG paragonites also have lower tetrahedral Al contents and slightly higher octahedral  $\text{Mg}+\text{Fe}^{2+}$  contents than pure paragonite (Fig. 5). The phyllosilicates are dioctahedral, with octahedral cations generally totalling 4.00 to 4.13 per  $\text{O}_{20}(\text{OH})_4$ . Beidellite and montmorillonite are dioctahedral smectites that form a continuous series, with the negative layer charge originating predominantly in tetrahedral sites in beidellite and in the octahedral layer in montmorillonite. The TAG paragonites trend toward smectite compositions close to the beidellite end-member (Fig. 5). In some samples, crystallites that exhibit zoning in BSE images contain variable proportions of smectite and paragonite on a fine scale (a few  $\mu\text{m}$ ), as indicated by varying interlayer cation totals. Total interlayer cation occupancies suggest that the phyllosilicates mostly contain 25%–60% smectite layers, but range up to ~85% smectite locally (Fig. 5).

Paragonite formed via replacement of chlorite in TAG stockwork samples, but there is no detectable difference in the composition of paragonite where it is directly replacing chlorite compared to paragonite farther from the reaction front or from other occurrences (Table 1). Intimate intergrowths of paragonite and chlorite are observed in BSE images at the scale of a few micrometers in several samples, however, and intergrowths of chlorite with paragonite at a scale finer than that observable by BSE images (see Pl. 8, Figs. 1 and 2), and electron microprobe analyses ( $<1 \mu\text{m}$ ) account for the elevated Fe,

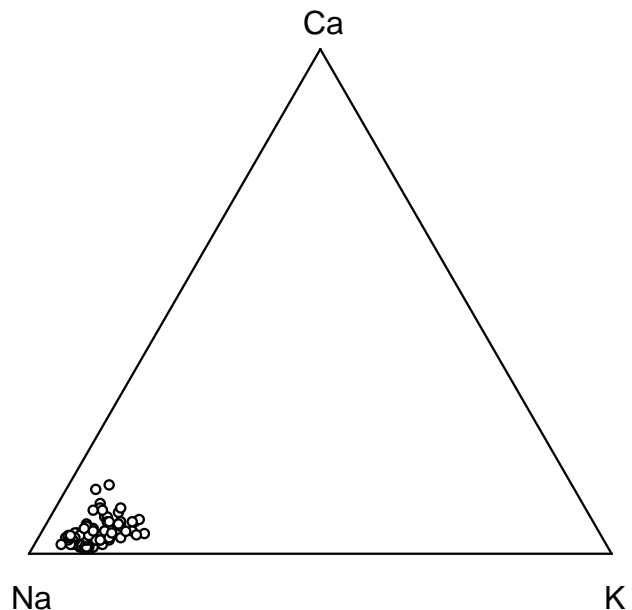


Figure 4. Interlayer cation compositions of TAG paragonites. Interlayer positions are dominated by Na. Formulas calculated on the basis of layer charge of 22 oxygens.

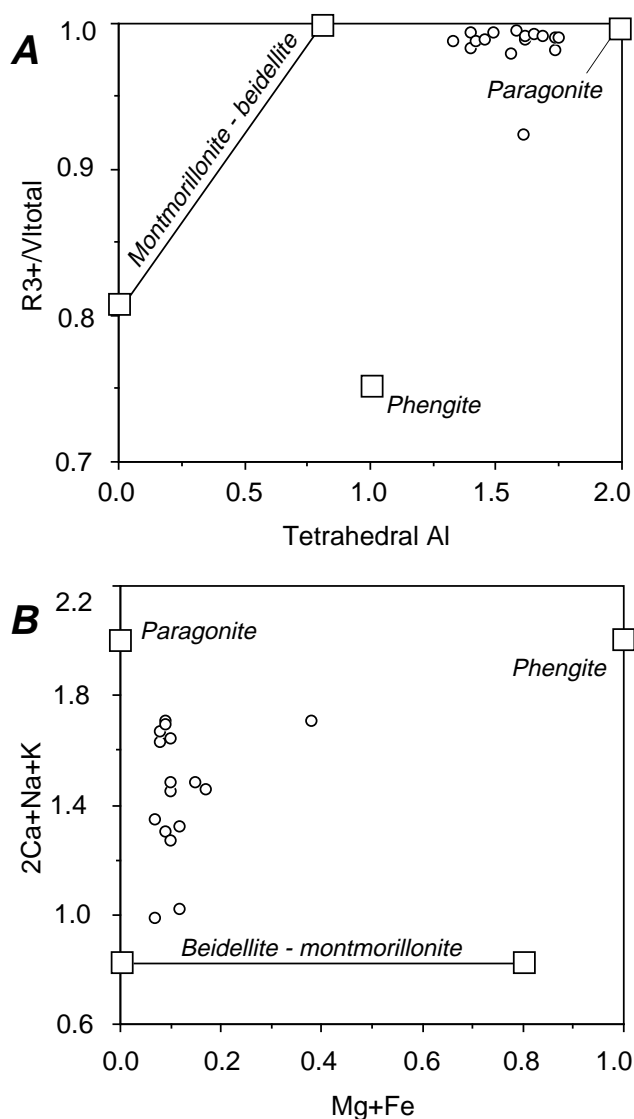


Figure 5. Compositions of TAG paragonites, formulas calculated on the basis of a layer charge of 22 oxygens. Open circles = paragonitic minerals; open boxes = end-member phyllosilicate compositions. **A.** TAG paragonites range to lower tetrahedral Al contents than end-member paragonite. Scatter to lower R<sup>3+</sup>/octahedral totals compared to pure paragonite is in part due to contamination by cryptocrystalline Ti-phase. **B.** Interlayer compositions of TAG paragonites; scatter to lower interlayer cation contents reflects the presence of smectite layers. The presence of relict chlorite layers could also contribute to this scatter, as well as increased octahedral totals.

Mg, and octahedral cation totals of some analyses (not plotted in Fig. 5).

Paragonite from one sample (Sample 158-957P 12R-2, Piece 15) has a relatively high Mg+Fe content, but also has high interlayer cation totals, suggesting a phengitic mica component (Fig. 5). The presence of chlorite causing the high Mg+Fe content of this sample can be ruled out, because this should lead to lower interlayer cation contents.

In one sample (Sample 158-957P 8R-1, 5–7 cm) some paragonite analyses were contaminated by a cryptocrystalline Cr-phase, that probably formed from breakdown of Cr-spinel in the rock. Electron microprobe analyses (<1 to 4 wt%; not plotted in Fig. 5) of nearby

paragonite contain high Cr, but it is uncertain whether these represent incorporation of Cr into a Cr-paragonite (a Na-fuchsite), or more probably represent analyses contaminated by the cryptocrystalline Cr-phase. Similarly, in contrast to paragonite in veins and filling open spaces which contains essentially no Ti, analyses of paragonite replacing basalt commonly contain significant amounts of TiO<sub>2</sub> (1 to 2 wt%; not plotted in Fig. 5). The high Ti contents are attributed to contamination by cryptocrystalline anatase, which was identified by X-ray diffraction in the intensely altered basalts. Other than these Ti- and Cr-contaminations no consistent difference was detected among paragonites from different occurrences: that is, precipitates in open spaces, replacing basalt, or among the different drill sites where paragonite was found (TAG-1, TAG-4, or TAG-5).

### Chlorite, Smectite, and Mixed-Layer Chlorite-Smectite Minerals

Chlorite from TAG exhibits a wide range of compositions, with distinct compositional fields for different sites beneath the mound (Fig. 6). Chlorites from the deep chloritic stockwork at TAG-1 are Fe-clinoclors having Fe/Fe+Mg = 0.3 to 0.5, which are more aluminous than other reported chlorites from the seafloor (Fig. 7). Bailey's (1980) classification of chlorites was used in this work. Variations in chlorite compositions are generally limited, but in some cases, significant differences occur on a small scale: in Sample 158-957E 18R-1, 4–7 cm, chlorite replacing a plagioclase phenocryst exhibits the full range of compositions detected in the deep chloritic stockwork. There are no consistent differences in compositions for different occurrences of chlorites in the deep stockwork in vesicles or veins, or replacing olivine, plagioclase, or groundmass. Nor was any difference detected between chlorite replacing basalts in the deep chloritic stockwork (i.e., early chlorite) and later chlorite in quartz + pyrite veins of the shallower paragonitic stockwork. A possible exception to this is chlorite at the reaction front where chlorite is being replaced by paragonite in Sample 158-957E 18R-1, 20–24 cm (see Pl. 8, Figs. 1 and 2). Here, chlorite in the rock and vein has a composition typical of the deep chloritic stockwork, but chlorite at the reaction front has higher Si, Na, and interlayer cation totals, indicating that paragonite layers are present at a scale finer than detected by BSE images. This may reflect the transition toward the compositions in equilibrium with the hydrothermal fluids, and also suggests that the chlorite at the reaction front is undergoing replacement and that it is only an intermediate step in the reaction and not in equilibrium with the hydrothermal fluids.

Chlorite replacing pillow rim glass from beneath the southeast margin of the mound at TAG-2 is a Mg-rich clinoclors (Fe/Fe+Mg = 0.17; Fig. 6). It is among the most magnesian chlorites reported from the seafloor (Fig. 7).

Chlorites in the chloritized alteration halos on basalts from beneath the northwest margin of the mound at TAG-4 are Mg-chamosites (Fig. 6), richer in Fe and higher in Si than chlorite from the deep chloritized stockwork. Trends of increasing Si contents and interlayer cation totals, and decreasing Al and Fe/Fe+Mg in phyllosilicates from the chloritized halos, are consistent with the presence of mixed-layer chlorite-smectite minerals (Fig. 6). These are similar to compositional trends observed for chlorite-smectite in typical seafloor metabasalts (Fig. 7).

Smectite in the host rocks beneath the margins of the mound at TAG-4 and TAG-2 are similar Mg-rich trioctahedral smectites (saponite), which range in composition from near talc to increasing Al and interlayer cation contents (Fig. 6B). These saponites fall within the range typical of smectites in seafloor basalts affected by low temperature alteration (0–150°C; Alt et al., 1986; Alt, 1995), but the low-charge smectites are also similar to stevensite replacing basalt associated with higher temperature (~200°C) hydrothermal venting (Zierenberg et al., 1995).

**Table 1. Representative electron microprobe analyses and structural formulas for paragonite, chlorite, smectite, and mixed-layer chlorite smectite.**

N:	5	608	32	41	605	132
Core, section, interval (cm):	957E-17R-1, 43-45	957B-4R-1, 29-38	957M-9R-1, 35-37	957M-10R-2, 17-19	957E-8R-1, 20-24	957E-18R-1, 41-43
	Chlorite (wt%)	Chlorite-smectite (replacing glass; wt%)	Chlorite-smectite (wt%)	Smectite (wt%)	Paragonite (wt%)	Paragonite (wt%)
SiO <sub>2</sub>	23.91	33.22	30.53	52.27	52.25	50.06
Al <sub>2</sub> O <sub>3</sub>	22.27	14.77	14.60	3.86	34.88	36.88
MgO	15.15	26.84	16.17	23.53	0.18	0.24
FeO	24.26	8.89	23.40	11.65	0.53	1.11
MnO	0.09	0.05	0.08	0.03	0.04	0.00
TiO <sub>2</sub>	0.06	0.00	0.04	0.00	0.09	0.03
CaO	0.06	0.22	0.64	0.78	0.36	0.40
Na <sub>2</sub> O	0.05	0.00	0.11	0.10	4.18	5.00
K <sub>2</sub> O	0.01	0.02	0.12	0.08	1.07	0.74
Total	85.85	84.01	85.69	92.31	95.44	94.46
Si	5.14	6.63	6.50	7.32	6.68	6.39
Al IV	2.86	1.37	1.50	0.64	1.32	1.61
Al total	5.64	3.47	3.66	0.64	5.25	5.54
Al VI	2.78	2.11	2.17		3.93	3.94
Mg	4.85	7.98	5.13	4.91	0.03	0.05
Fe <sup>S+</sup>	4.35	1.48	4.16	1.36	0.06	0.12
Mn	0.02	0.01	0.01	0.00	0.00	0.00
Ti	0.01	0.00	0.01	0.00	0.01	0.00
VI total	12.01	11.58	11.48		6.27	4.10
Ca	0.01	0.05	0.15	0.12	0.05	0.05
Na	0.02	0.00	0.05	0.03	1.03	1.23
K	0.00	0.01	0.03	0.01	0.17	0.12
Ca+Na+K	0.04	0.05	0.23	0.16	1.25	1.41
Fe/Fe+Mg	0.473	0.156	0.448	0.217	0.62	0.72

Notes: Formulas calculated on the basis of a layer charge of 28 oxygens for chlorites and mixed-layer chlorite-smectites, and on 22 oxygens for paragonites. All iron as ferric iron.

Several analyses of mixed-layer chlorite-smectites from TAG-4 fall in the intermediate areas of the trends between smectite and chlorite in Figures 6A and 6B but are not plotted because the analyses were contaminated by Ti oxides. These data indicate that a continuous series of mixed-layer chlorite-smectite probably exists between chlorite and smectite in the alteration halos and host rocks at TAG-4.

### Talc

In the lowest sections of Holes 158-957B and 957M, in TAG-2 and TAG-4 areas, respectively, talc was identified in several samples of slightly altered (3–15 vol%) dark gray basalt in which olivine microphenocrysts are fresh or partly replaced by, and vesicles and interstitial voids are filled with saponite-talc mixtures. Talc was identified on the basis of optical properties (colorless in plane polarized light, high birefringence between crossed polarizers), X-ray diffraction, and electron microprobe analyses (see paragraph above and Figs. 6A, 6B, 7). High Fe contents of talc-rich samples (FeO total up to 8 wt%) suggest the presence of Fe-rich talc as observed in other altered seafloor rocks (Shau and Peacor, 1992).

## DISCUSSION

### Sequence of Alteration Processes

The petrographic and mineralogical study of the variously altered basaltic fragments observed in the cores drilled during Leg 158 allow the reconstruction of the sequence of alteration processes. The sequence is not complete in any single sample and not even in any one section drilled through the TAG active mound. The following complete alteration sequence is compiled from observations of all of the studied samples.

Basement beneath the mound margins (Hole 957B on the southeast and Hole 957M on the west) contains the least altered rocks, as well as hydrothermally altered rocks. The dark gray basalt cores, sporadically surrounded by variously colored alteration halos, contain minor amounts of smectite and rare iddingsite partially replacing oli-

vine crystals and filling cracks, vesicles, and miarolitic voids. On the other hand, plagioclase microlites, plumose clinopyroxenes, and Cr-spinel crystals are generally unaltered. Such basaltic basement samples from the distal drill holes have been affected by a very slight alteration by cold, oxidizing seawater without having undergone the various hydrothermal alteration stages listed below.

The first stage of hydrothermal alteration is the chloritization of the basaltic basement as a result of interaction, at high temperature, with Mg-bearing hydrothermal solutions. Chloritization processes differed, however, in basement beneath the southeastern portion of the mound (TAG-2 area) compared to the western mound margin (TAG-4 area), and both differ from the central, deeper chloritic stockwork (TAG-1 area). The basal part of distal Hole 957B (TAG-2 area) contains, besides slightly altered smectite-bearing dark gray basalts (see above), chloritized rocks that differ from those in the deep, central chloritic stockwork. In the lower portion of distal Hole 957M (TAG-4 area), the slightly altered, smectite-bearing, dark gray basalts are bordered by cm-wide chloritized alteration halos surrounded by millimeter-thick outer red halos. In the deepest section reached by drilling in the central TAG-1 area, near the present-day fluid up-flow zone, pervasive chloritization generated greenstones in which all of the primary minerals, except Cr-spinel, are replaced by chlorite, with minor quartz and pyrite. In most of the chloritized rocks, the sequence of secondary minerals precipitation in veins and vesicles is with chlorite, followed by quartz and pyrite. Calculated slight gains of Mg by chloritized rocks and O and Sr isotope data indicate reaction with end-member fluids having a slight seawater component, that is, Mg-bearing hydrothermal solutions at temperatures of about 300°C (Alt and Teagle, Chap. 21, this volume; Teagle et al., Chap. 22, this volume).

The second stage of hydrothermal alteration is the paragonitization, silicification, and pyritization of the basalt clasts. During this stage, earlier formed clay minerals (i.e., chlorite, smectite, and chlorite-smectite mixed-layer minerals) as well as the relict primary minerals were replaced by paragonite. The typical white mica characteristic of sericitization of the host-rocks associated with land-based and a few other oceanic massive sulfide deposits is K-rich. However, it is

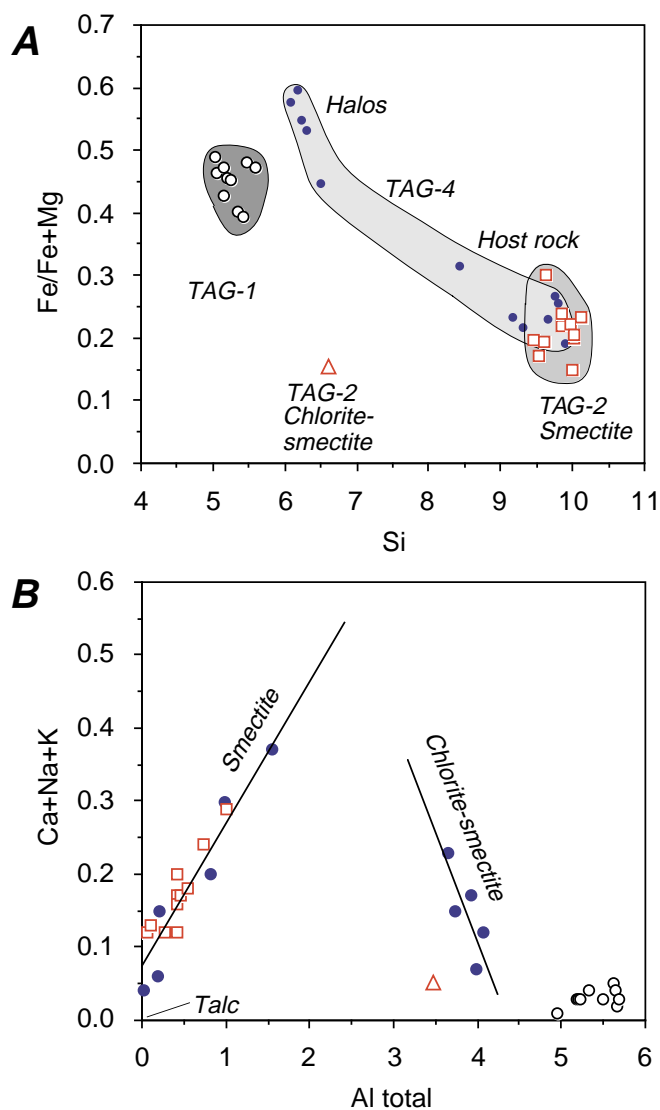


Figure 6. **A.** TAG chlorite, talc, smectite and mixed-layer chlorite-smectite compositions. Formulas calculated on the basis of a layer charge of 28 oxygens. Open circles = chlorites from TAG-1; solid circles = chlorites, mixed-layer chlorite-smectite minerals, and smectites from TAG-4; open boxes = smectites from TAG-2; open triangle = mixed-layer chlorite-smectite mineral from TAG-2. Chlorites from different drill sites beneath the mound fall in distinct fields. Chlorite in a plagioclase pseudomorph from TAG-1 exhibits the full range of compositional variation for this site (see Pl. 8, Fig. 3). Chlorite in the vein shown in Pl. 8, Figs. 1 and 2, has a composition typical for the TAG-1 site, but chlorite at the reaction front where it is being replaced by paragonite (Plate 8, Figure 2) has higher Fe/Fe+Mg and Si (solid squares). Chlorites, mixed-layer chlorite-smectite (+talc), and smectite-talc in chloritized alteration halos and host rocks from Hole 957M exhibit trend of decreasing Fe and increasing Mg and Si. Smectite and smectite-talc from Hole 957B shown for comparison. **B.** Interlayer cation contents vs. Al for TAG chlorite, talc, smectite, and mixed-layer chlorite-smectite (same symbols as in Fig. 6A). Formulas calculated on the basis of a layer charge of 28 oxygens. Chlorite being replaced by paragonite at the reaction front is not represented because it has higher interlayer cation contents, reflecting the presence of paragonite at a scale finer than the microprobe analysis (~1  $\mu$ m). Arrow indicates trend toward paragonite composition. Chlorite and mixed-layer chlorite-smectite from alteration halos in Hole 957M trends toward smectite, but the low interlayer cation contents indicate that talc is also present in the mixed layer samples. At higher Si contents, interlayer cations decrease toward talc compositions in the less altered host rocks.

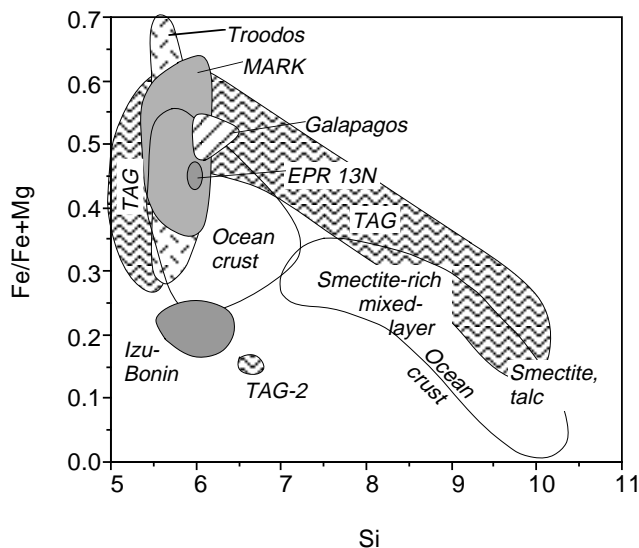


Figure 7. TAG chlorite compositions compared to those of chlorites and chlorite-smectite-talc mixed-layer phyllosilicates from other hydrothermally altered oceanic rocks.

not surprising to find a Na-rich silicate of aluminum as an alteration product of basaltic basement forming the stockwork under the TAG active sulfide mound because of the high Na/K ratio of the present-day hydrothermal fluids discharged by the TAG black smokers compared to those of other black smokers (Von Damm, 1995). Such a high Na/K ratio shifts the present day TAG hydrothermal fluid composition to the stability field of paragonite from that of muscovite corresponding to the lower Na/K ratios of black smoker fluids from the other localities. Moreover, crystallization temperatures of up to 360°C similar to those of the TAG black smoker fluid were inferred from the O isotope analyses of the quartz associated with paragonite (Alt and Teagle, Chap. 21, this volume). The hydrothermal fluid generating the paragonite was Mg-poor.

The second stage of hydrothermal alteration was also responsible for intense silicification and pyritization of the basaltic rocks. It was probably concomitant with the paragonitization process described above. Petrographic observations in and around the basaltic clasts, of disseminated euhedral pyrite crystals surrounded by quartz coronas and frequently zoned quartz + pyrite veins confirm that the basaltic stockwork was affected by recurrent silicification and pyritization. This process led to the “explosion” of the basalt clasts, probably through hydrofracturing and infilling of the fractures by quartz and pyrite. As a consequence, the clasts “melted” away into the quartz + pyrite matrix of the various types of silica-pyrite breccias which form, by far, most of the massive sulfide mound. Pyritization appears to have been the most intense in Hole 957P section through the TAG-5 area near the northern margin of the mound.

As a result of hydrothermal alteration stage 2, the basaltic primary minerals and textures were progressively erased and replaced by mixtures of “dirty” quartz, pyrite, and interstitial paragonite which are extremely difficult to distinguish from the directly precipitated quartz + pyrite + paragonite matrix of the pyrite-silica breccias. The most resistant primary mineral is the Cr-spinel that is still commonly observed in the completely chloritized basalt samples but has disappeared in the paragonitized, silicified and pyritized clasts. However, Cr-rich paragonites were found in interstitial position among “dirty” quartz and pyrite crystals cementing strongly hydrothermally altered chloritized basalt clasts, and as replacement product after basalt clasts. At the present stage of our study, it is not possible to say whether a Cr-bearing paragonite analogous to fuchsite, i.e., the Cr-bearing muscovite, formed in the TAG mound. The end product of

this intense and pervasive alteration of the basaltic basement by high temperature hydrothermal solutions are mixtures of various proportions of quartz, pyrite and paragonite from which hydrothermally "incompatible" elements have been leached away and only Fe, S, Si, Al, and Na with some Cr and Ti remain, forming the hydrothermal minerals.

The last stage of hydrothermal mineralization corresponds to anhydrite precipitating in open spaces such as veins, voids in the breccia matrix, or on exposed sample surfaces. Anhydrite precipitation results from the entrainment of seawater into the hot hydrothermal system.

Finally, some of the basalt fragments from the basement under the margins of the mound (e.g., TAG-4 area) and displaying green chloritized halos resulting from the first stage of hydrothermal alteration, were later altered by cold seawater. As a consequence these halos are now stained red by Fe-oxyhydroxides replacing the disseminated pyrite that was associated with the chlorite. The low temperature of this "submarine weathering" process is confirmed by oxygen isotope analyses (Alt and Teagle, Chap. 21, this volume).

### WHY ARE THE CLASTS FOUND SO HIGH ABOVE THE INFERRED BASEMENT LEVEL UNDER THE MOUND?

Hydrothermally altered basalt clasts were found at shallow depths in the TAG-1 central area, 84, 81 and 42 m above the hydrothermally altered stockwork, that is, 16, 20 and 49 mbsf, in Holes 957G, 957C, and 957E, respectively (see "Alteration Lithostratigraphy" section and Fig. 3). Similarly, beneath the distal margins of the mound, hydrothermally altered basalt clasts were observed at depths as shallow as 0.74 mbsf (i.e., 41 m above the chloritized basement in TAG-4 Hole 957M). What process could have transported the clasts so high in the mound, several tens of meters above the depth of the initial ocean floor inferred from the depth of the plane surface connecting the tops of the basement encountered in the distal drill holes? Several mechanisms could be responsible for transporting basalt clasts from the basement to or near the mound surface. Among these mechanisms are entrainment in high-velocity hydrothermal fluid, processes analogous to "frost jacking and heave," and the nearly complete replacement of basement.

Hydrothermal fluid flow rates up to several meters per second have been measured at black smoker chimney vents (e.g., Converse et al., 1984), implying that fluid discharge with similar velocities have to prevail in the subsurface upflow zones of seafloor hydrothermal systems. Such high flow rates could result from the confinement of the hydrothermal solutions along fault zones and other fissures which channel them toward the surface. Near the seafloor, the hydrothermal solutions are even more focused into vents restricted by the cooling-induced precipitation of secondary minerals that throttle the conduit ("garden hose effect") and might end up in completely sealing the exit vents. This mechanism was discussed by Delaney et al. (1987), who considered it to be responsible for the formation of quartz-cemented, pyrite-bearing greenstone breccias recovered by dredging and submersible from the Mid-Atlantic Ridge near its southern intersection with the Kane Fracture. Clasts in the greenstone breccias range in size from 0.01 to 1.5 cm. Calculations based on Shields's criterion (1936; in Delaney et al., 1987) for threshold conditions of particles set in motion by Newtonian fluid during sediment motion show that clasts 1 cm in diameter would require conduit flow rates of about 1 m/s to achieve minimum entrainment. This flow rate is the same order of magnitude as that measured in black smokers exiting from the central TAG chimneys. Rock fragments were recently observed being transported above the seafloor by hydrothermal solutions flowing out of a man-made hole into a hydrothermal site. According to an October 1996 ODP press release, as Hole 1035F was being drilled during Leg 169, "hot (286°C) water was rushing out of

the hole so fast that it was carrying mud and rock fragments (i.e., drill cuttings of up to 2 cm for sediments and 5 mm for sulfides) and forming a cloud more than 30 m above the seafloor."

When, in winter, soil interstitial water migrates into a freezing front, it forms ice lenses that take more volume than when water is liquid in summer. "Frost heave" involves actual migration of unfrozen water into the freezing front, followed by freezing into ice lenses in winter. Fine-grained frozen soils still contain unfrozen water at sub-zero temperatures because of surficial tension in fine pores. Water is drawn into these fine-grained soils as they freeze, and the resulting volume expansion of the soil is often much greater than the expansion caused by the water-ice transition alone. Ice forms in a direction that maximizes energy lost, i.e., upwards with the geothermal gradient, and by volumetric increase at the ice/water phase boundary, it expands toward the least resistance, i.e., free surface. This results in a "frost mound," i.e., a general but uneven lifting of the ground surface and any overlying structures such as pavement. On the other hand, "frost jacking or thrusting" is a mechanism by which rock from pebbles to boulders are uplifted to the ground surface through permafrost and other periglacial soils. The frost heave-related volumetric increase displaces toward the ground surface whatever object the soil had trapped when freezing, e.g., rock fragments. When the frost melts during the next warm season, the rock fragments are left behind, i.e., higher relative to their original position. Moreover, upon thawing of the soil which froze to the sides of objects, the meltwater-washed sediment infills spaces below the uplifted object and the latter will not move back downwards as much. Both frost heave and frost jacking processes are related and often concomitant. The processes are regularly repeated every year and the rock fragments progressively move toward the ground surface until they finally outcrop (Williams and Smith, 1977 in Williams and Fremont, 1977; Anderson-Duwayne and Williams, 1985 and ref. therein). Similarly, one can imagine that basalt clasts could progressively move up from the basement beneath the TAG mound when the host basalt of the stockwork is replaced by lower density pyrite + quartz + paragonite breccias with lower bulk densities as a result of repeated hydrofracturing. The cracks would then fill and replace the clasts with hydrothermal minerals during the second hydrothermal alteration stage. Alternatively, the recurrent succession of anhydrite precipitation during the last hydrothermal stage ( $0.4 \times 10^6$  tons of anhydrite are estimated in the TAG mound) and later dissolution (anhydrite dissolves whenever hydrothermal activity stops and cold seawater seeps through the mound) in pore spaces and fissures within the sulfide-rich mound could mimic the effects of repeated freezing and thawing of water during "frost heave and frost jacking." As a consequence of its dissolution at low temperature, anhydrite is not found in ancient land-based VMS deposits which, on the other hand, often display brecciated, cavity filling, and collapse structures both in the massif sulfide and the underlying "propylitized" stockwork. Volume change calculations taking into account the various mineral phase densities and their proportions within the various types of breccias are needed to confirm the feasibility of the "frost heave and frost jacking" hypothesis.

The last process is probably the most difficult to demonstrate. The presence of hydrothermally altered basalt clasts above the level of the basement could be explained by an almost complete replacement of a basaltic mound by the siliceous pyrite breccias as a result of an extremely intense hydrothermal alteration. Such a process would leave in situ only a few small relicts of deeply altered basalt in quartz + pyrite + paragonite mixtures, and the top of the easily recognizable basement would effectively sink below its original level down to where the stockwork was encountered by drilling. This hypothesis implies that the inferred basement surface was neither flat nor plane but that the hydrothermal mound was superimposed on a now obscured dome-shaped volcanic edifice similar to those observed nearby in the TAG hydrothermal field (Rona et al., 1993), consistent with Lisitsyn's et al. (1989) hypothesis (see "Alteration Lithostratigraphy" section, this chapter). Such volcanic edifices do not appear to be

petrochemically different from the adjacent basaltic seafloor. However, one could ask the question why hydrothermal discharge would preferentially take place through a thicker volcanic sequence when the pathway of least hydrodynamic resistance would probably be located at the margins of such an edifice.

## ACKNOWLEDGMENTS

W. Goodfellow, J. Miller and P. Schiffman are gratefully acknowledged for their critical reviews and insightful comments. We thank R. Knott who provided assistance on many occasions. We thank the crew and engineers who participated in Leg 158. This work was supported by the Géosciences Marines program of the Institut National des Sciences de l'Univers, France, and the National Science Foundation, USA.

## REFERENCES

- Alt, J.C., 1994. A sulfur isotopic profile through the Troodos ophiolite, Cyprus: primary composition and the effects of seawater hydrothermal alteration. *Geochim. Cosmochim. Acta*, 58:1825–1840.
- , 1995. Subseafloor processes in mid-ocean ridge hydrothermal systems. In Humphris, S.E., Zierenberg, R., Mullineaux, L., and Thomson, R. (Eds.), *Seafloor Hydrothermal Systems: Physical, Chemical, Biological and Geological Interactions within Hydrothermal Systems*. Geophys. Monogr., Am. Geophys. Union, 91:85–114.
- Alt, J.C., and Jiang, W.T., 1991. Hydrothermally precipitated mixed-layer illite-smectite in recent massive sulfide deposits from the seafloor. *Geology*, 19:570–573.
- Alt, J.C., Lonsdale, P., Haymon, R., and Muehlenbachs, C., 1987. Hydrothermal sulfide and oxide deposits on seamounts near 21°N, East Pacific Rise. *Geol. Soc. Am. Bull.*, 98:157–168.
- Alt, J.C., Muehlenbachs, K., and Honnorez, J., 1986. An oxygen isotopic profile through the upper kilometer of the oceanic crust, DSDP Hole 504B. *Earth Planet. Sci. Lett.*, 80:217–229.
- Anderson-Dewayne, M., and Williams, P.J. (Eds.), 1985. Freezing and thawing of soil-water systems. *Am. Soc. Civ. Eng.*
- Bailey, S.W., 1980. Summary of recommendations of AIPEA Nomenclature Subcommittee. *Clays Clay Miner.*, 15:85–89.
- Becker, K., and Von Herzen, R.P., 1996. Pre-drilling observations of conductive heat flow at the TAG active mound using *Alvin*. In Humphris, S.E., Herzig, P.M., Miller, D.J., et al., *Proc. ODP, Init. Repts.*, 158: College Station, TX (Ocean Drilling Program), 23–29.
- Bideau, D., and Hekinian, R., 1984. Segregation vesicles of ocean floor basalts, 1: Petrological study of the segregation products. *J. Geophys. Res.*, 89:7903–7914.
- Bonatti, E., Honnorez-Guerstein, B.M., and Honnorez, J., 1976. Copper iron sulfide mineralizations from the Equatorial Mid-Atlantic Ridge. *Econ. Geol.*, 71:1515–1525.
- Converse, D.R., Holland, H.D., and Edmond, J.M., 1984. Flow rates in the axial hot springs of the East Pacific Rise (21°N): implications for the heat budget and the formation of massive sulfide deposits. *Earth Planet. Sci. Lett.*, 69:159–175.
- Delaney, J.R., Mogk, D.W., and Mottl, M.J., 1987. Quartz-cemented breccias from the Mid-Atlantic Ridge: samples of a high-salinity hydrothermal upflow zone. *J. Geophys. Res.*, 92:9175–9192.
- Edmond, J.M., Campbell, A.C., Palmer, M.R., German, C.R., Klinkhammer, G.P., Edmonds, H.N., Elderfield, H., Thompson, G., and Rona, P., 1995. Time-series studies of vent fluids from the TAG and MARK sites (1986, 1990), Mid-Atlantic Ridge: a new solution chemistry model and a mechanism for Cu/Zn zonation in massive sulfide ore bodies. In Parson, L.M., Walker, C.L., and Dixon, D.R. (Eds.), *Hydrothermal Vents and Processes*. Geol. Soc. Spec. Publ. London, 87:77–86.
- Edmond, J.M., Measures, C., McDuff, R.E., Chan, L.H., Collier, R., and Grant, B., 1979. Ridge crest hydrothermal activity and the balances of the major and minor elements in the ocean: the Galapagos data. *Earth Planet. Sci. Lett.*, 46:1–18.
- Embley, R.W., Jonasson, I.R., Perfit, M.R., Franklin, J.M., Tivey, M.A., Malahoff, A., Smith, M.F., and Francis, T.J.G., 1988. Submersible investigation of an extinct hydrothermal system on the Galapagos Ridge: sulfide mounds, stockwork zone, and differentiated lavas. *Can. Mineral.*, 26:517–539.
- Guidotti, C.V., Sassi, F.P., Blencoe, J.G., and Selverstone, J., 1994. The paragonite-muscovite solvus: I. P-T-X limits derived from the Na-K compositions of natural, quasibinary paragonite-muscovite pairs. *Geochim. Cosmochim. Acta*, 58:2269–2276.
- Harper, G.D., Bowman, J.R., and Kuhns, R.J., 1988. A field, chemical, and stable isotope study of subseafloor metamorphism of the Josephine Ophiolite, California-Oregon. *J. Geophys. Res.*, 93:4625–4656.
- Haymon, R.M., and Kastner, M., 1986. The formation of high temperature clay minerals from basalt alteration during hydrothermal discharge on the East Pacific Rise axis at 21°N. *Geochim. Cosmochim. Acta*, 50:1933–1939.
- Honnorez, J., Alt, J.C., Honnorez-Guerstein, B.-M., Laverne, C., Muehlenbachs, K., Ruiz, J., and Saltzman, E., 1985. Stockwork-like sulfide mineralization in young oceanic crust: Deep Sea Drilling Project Hole 504B. In Anderson, R.N., Honnorez, J., Becker, K., et al., *Init. Repts. DSDP*, 83: Washington (U.S. Govt. Printing Office), 263–282.
- Humphris, S.E., Herzig, P.M., Miller, D.J., et al., 1996. *Proc. ODP, Init. Repts.*, 158: College Station, TX (Ocean Drilling Program).
- Karson, J.A., and Rona, P.A., 1990. Block tilting, transfer faults, and structural control of magmatic and hydrothermal processes in the TAG area, Mid-Atlantic Ridge 26°N. *Geol. Soc. Am. Bull.*, 102:1635–1645.
- Kirkpatrick, R.J., 1978. Processes of crystallization in pillow basalts, Hole 396B, DSDP Leg 46. In Dmitriev, L., Heirtzler, J., et al., *Init. Repts. DSDP*, 46: Washington (U.S. Govt. Printing Office), 271–282.
- Kleinrock, M.C., Humphris, S.E., and the Deep-TAG Team, 1996. Detailed structure and morphology of the TAG active hydrothermal mound and its geotectonic environment. In Humphris, S.E., Herzig, P.M., Miller, D.J., et al., *Proc. ODP, Init. Repts.*, 158: College Station, TX (Ocean Drilling Program), 15–21.
- Lalou, C., Reyss, J.-L., Bricchet, E., Rona, P.A., and Thompson, G., 1995. Hydrothermal activity on a 10<sup>5</sup>-year scale at a slow-spreading ridge, TAG hydrothermal field, Mid-Atlantic Ridge 26°N. *J. Geophys. Res.*, 100:17855–17862.
- Lisitsyn, A.P., Bogdanov, Y.A., Zonenshayn, L.P., Kuz'min, M.I., and Sagalevich, A.M., 1989. Hydrothermal phenomena in the Mid-Atlantic Ridge at Lat. 26°N (TAG hydrothermal field). *Int. Geol. Rev.*, 31:1183–1198.
- Masuda, H., Chiba, H., Gamo, T., Fujioka K., and Nakamura, M., 1995. Distribution and chemical characteristics of hydrothermal alteration minerals recovered from the TAG active mound, MAR 26°N. *JAMSTEC J. Deep Sea Res.*, 11:111–124.
- Mills, R.A., Clayton, T., and Alt, J.C., 1996. Low-temperature fluid flow through sulfidic sediments from TAG: modification of fluid chemistry and alteration of mineral deposits. *Geophys. Res. Lett.*, 23:3495–3498.
- Mills, R.A., and Elderfield, H., 1995. Rare earth element geochemistry of hydrothermal deposits from the active TAG mound, 26°N Mid-Atlantic Ridge. *Geochim. Cosmochim. Acta*, 59:3511–3524.
- Mottl, M.J., 1983. Metabasalts, axial hot springs, and the structure of hydrothermal systems at mid-ocean ridges. *Geol. Soc. Am. Bull.*, 94:161–180.
- Nehlig, P., Juteau, T., Bendel, V., and Cotten, J., 1994. The root zone of oceanic hydrothermal systems: constraints from the Samail ophiolite (Oman). *J. Geophys. Res.*, 99:4703–4713.
- Richards, H.G., Cann, J.R., and Jensenius, J., 1989. Mineralogical zonation and metasomatism of the alteration pipes of Cyprus sulfide deposits. *Econ. Geol.*, 84:91–115.
- Richardson, C.J., Cann, J.R., Richards, H.G., and Cowan, J.G., 1987. Metal-depleted root zones of the Troodos ore-forming hydrothermal systems, Cyprus. *Earth Planet. Sci. Lett.*, 84:243–253.
- Rona, P.A., Hannington, M.D., Raman, C.V., Thompson, G., Tivey, M.K., Humphris, S.E., Lalou, C., and Petersen, S., 1993. Active and relict seafloor hydrothermal mineralization at the TAG hydrothermal field, Mid-Atlantic Ridge. *Econ. Geol.*, 88:1987–2013.
- Rona, P.A., and Trivett, D.A., 1992. Discrete and diffuse heat transfer at ASHES vent field, Axial Volcano, Juan de Fuca Ridge. *Earth Planet. Sci. Lett.*, 109:57–71.
- Saccoccia, P.J., and Gillis, K.M., 1995. Hydrothermal upflow zones in the oceanic crust. *Earth Planet. Sci. Lett.*, 136:1–16.
- Saccoccia, P.J., and Seyfried, W.E., 1995. The solubility of chlorite solid solutions in 3.2 wt% NaCl fluids from 300–400°C, 500 bars. *Geochim. Cosmochim. Acta*, 58:567–585.
- Schiffman, P., Smith, B.M., Varga, R.J., and Moores, E.M., 1987. Geometry, conditions, and timing of off-axis hydrothermal metamorphism and ore-deposition in the Solea Graben. *Nature*, 325:423–425.
- Schultz, A., Delaney, J.R., and McDuff, R.E., 1992. On the partitioning of heat flux between diffuse and point-source seafloor venting. *J. Geophys. Res.*, 97:12299–12314.

- Seyfried, W.E., and Ding, K., 1995. Phase equilibria in seafloor hydrothermal systems: a review of the role of redox, temperature, pH and dissolved Cl on the chemistry of hot spring fluids at mid-ocean ridges. In Humphris, S., Lupton, J., Mullineaux, L., and Zierenberg, R. (Eds.), *Physical, Chemical, Biological and Geological Interactions Within Submarine Hydrothermal Systems*. Am. Geophys. Union, Geophys. Monogr., 91:248–272.
- Shau, Y.H., and Peacor, D.R., 1992. Phyllosilicates in hydrothermally altered basalts from DSDP Hole 504B, Leg 83: a TEM and AEM study. *Contrib. Mineral. Petrol.*, 112:119–133.
- Shields, A., 1936. Anwendung der Ähnlichkeits Mechanik und der Turbulenzforschung auf die Geschiebebewegung. *Mitt. Preuss. Versuchsanst. Wasser Schiffss.*, 26:26.
- Tivey, M., Humphris, S.E., Thompson, G., Hannington, M.D., and Rona, P.A., 1995. Deducing patterns of fluid flow and mixing within the TAG active hydrothermal mound using mineralogical and geochemical data. *J. Geophys. Res.*, 100:12527–12555.
- Tivey, M.A., Rona, P.A., and Schouten, H., 1993. Reduced crustal magnetization beneath the active sulfide mound, TAG hydrothermal field, Mid-Atlantic Ridge 26°N. *Earth Planet. Sci. Lett.*, 115:101–115.
- Von Damm, K.L., 1995. Controls on the chemistry and temporal variability of seafloor hydrothermal fluids. In Humphris, S.E., Zierenberg, R.A., Mullineaux, L.S., and Thomson, R.E. (Eds.), *Seafloor Hydrothermal Systems: Physical, Chemical, Biological, and Geological Interactions*. Am. Geophys. Union, 91:222–247.
- Williams, P.J., and Fremond, M. (Eds.), 1977. Soil freezing and highway construction, Carleton Univ., Ottawa. *Ont. Ecole Nat. Ponts Chaussées*.
- Zierenberg, R.A., Schiffman, P., Jonasson, I.R., Tosdal, R., Pickthorn, W., and McClain, J., 1995. Alteration of basalt hyaloclastite at off-axis Sea Cliff hydrothermal field, Gorda Rise. *Chem. Geol.*, 126:77–99.

**Date of initial receipt: 4 June 1996**

**Date of acceptance: 4 April 1997**

**Ms 158SR-219**

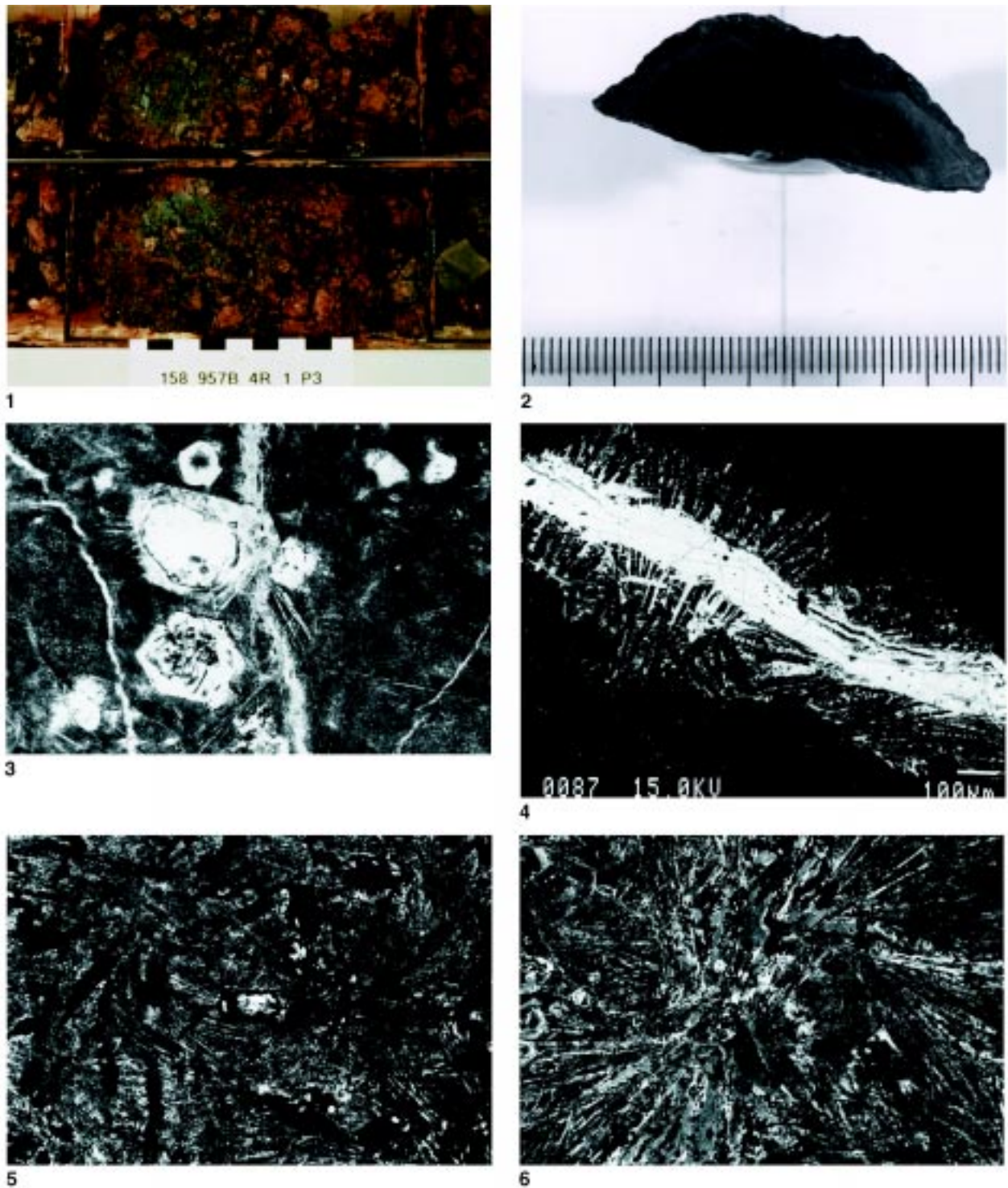


Plate 1. Basalts from distal Hole 957B into the TAG-2 southeast basement. **1.** Samples 158-957B-4R-1 (Piece 2 to Piece 4, 15–43 cm) of chloritized basalt fragments and pillow breccia. The basalt fragments display red chloritic and hematitic alteration halos around dark gray, slightly altered cores, whereas the pillow breccia (i.e., Piece 3) is made up of chlorite, hematite, and quartz. **2.** Sample 158-957B-4R-1 (Piece 6, 43–50 cm) of aphyric basalt exhibits a 5- to 7-mm thick reddish brown halo around a slightly altered dark gray core. **3.** Photomicrograph of slightly altered dark gray basalt inner core from Sample 158-957B-4R-1 (Piece 7, 51–54 cm); smectite fills vesicles (e.g., upper center), vugs (upper right and lower left corners), and veins (the largest one is about 0.1 to 0.15 mm thick), and partly replaces the two olivine microphenocrysts. Uncrossed polars, field of view = 1.5 mm. **4.** Backscatter electron photomicrograph of a diffuse hematite + lepidocrosite vein (0.3 to 0.5 mm thick) in the outer reddish brown halo of Sample 158-957B-4R-1 (Piece 6, 48–49 cm). **5.** Photomicrograph of a reddish brown outer halo in Sample 158-957B-5R-1 (Piece 2, 7–9 cm) showing a smectite + iddingsite pseudomorph after an olivine microphenocryst (at center) and numerous Fe-oxyhydroxide replacement of plagioclase microlites. Uncrossed polars, field of view = 1.5 mm. **6.** Photomicrograph of slightly altered dark gray inner core of the same sample as above showing unaltered plagioclase microlites (white), cryptocrystalline groundmass (gray), and opaques, whereas the glomerophytic olivine microphenocryst aggregate, in center left, is replaced by smectite. Uncrossed polars, field of view = 1.5 mm.



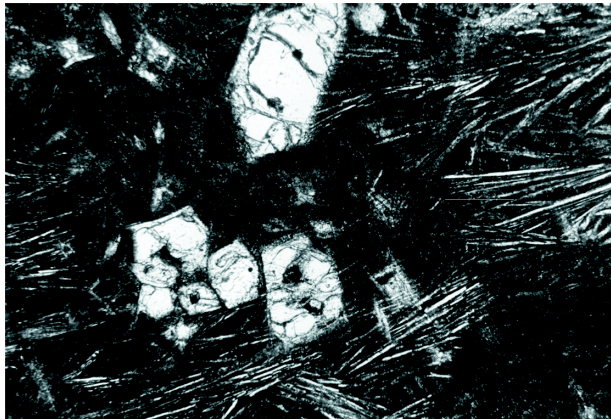
1



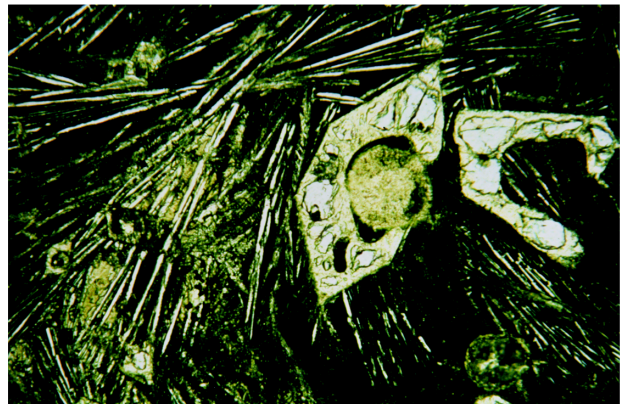
2



3



4



5

Plate 2. Basalt samples from distal Hole 957M into TAG-4 northwest basement. **1.** Sample 158-957M 9R-1, (Piece 6, 31–37 cm) exhibits a 1-cm-thick, outer green chloritized halo concentric with 2-mm-thick, inner black halos surrounding an inner, unaltered dark gray core. **2.** Sample 158-957M-10R-1, (Piece 21, 140–146 cm) shows an outer, 2- to 3-mm-thick, green, chloritized halo surrounding an inner, 1- to 2-mm thick, black halo around a unaltered dark gray core. Notice, in both samples, the sharp contacts of the black halos against the unaltered inner cores, whereas their contacts with the outer green halos are diffused. **3.** Three basalt samples displaying the variolitic texture characteristic of pillow rims. The sample on the left, Sample 158-957M-9R-1, (Piece 3, 13–18 cm), and the sample on the right, Sample 158-957M-10R-2, (Piece 7, 31–34 cm), are pervasively chloritized and crossed by a 2-mm-thick vuggy pyrite vein (in the left sample) or a 2-mm-thick pyrite + quartz vein bordered with a double light-dark chloritic halos (in the right sample). Sample 158-957M-9R-1 (Piece 8, 45–52 cm), in center, is slightly altered and contains smectite. **4.** Photomicrograph of Sample 158-957M-9R-1 (Piece 12, 72–79 cm) shows euhedral olivine microphenocrysts slightly altered to smectite, in an unaltered subvariolitic groundmass. Uncrossed polars, field of view = 1.5 mm. **5.** Chlorite-smectite mixture almost completely replacing two skeletal olivine microphenocrysts and filling miarolitic voids (center-left and upper right corner) and vesicles (in center and upper left corner) in the green, outer halo of Sample 158-957M-10R-1 (Piece 9, 61–66 cm). Uncrossed polars, field of view = 1.5 mm.

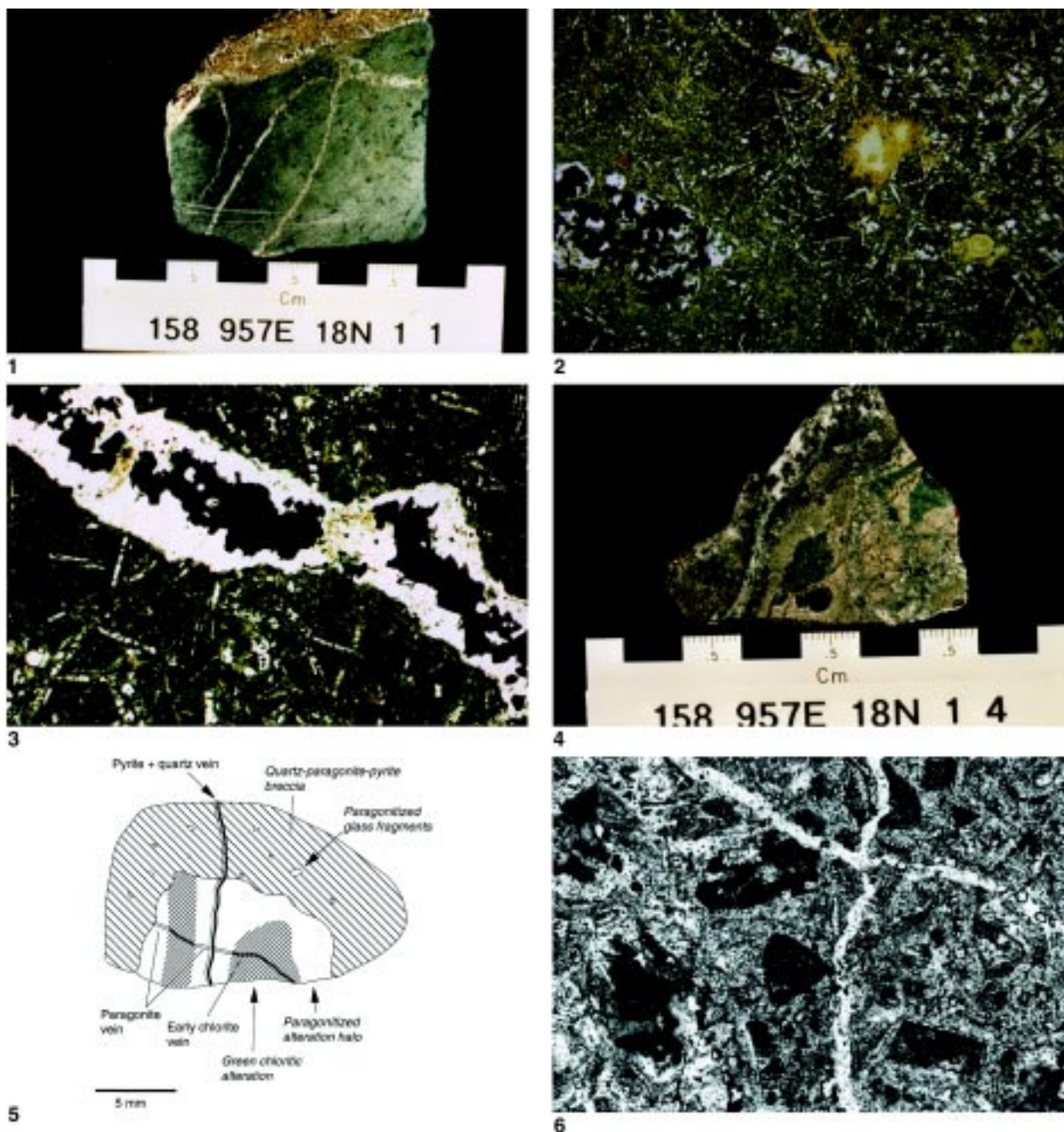


Plate 3. Chloritization and transition to paragonite + quartz + pyrite alteration from the deeper, central part of the mound. **1.** Chloritized basalt Sample 158-957E-18R-1 (Piece 1, 0–8 cm) crossed by four 0.005- to 1-mm-thick quartz + pyrite + chlorite (together or alone) veins and bordered by a 1-cm-thick pyrite + anhydrite vein. Dark spots in the host rock are chlorite pseudomorphs after olivine and plagioclase microphenocrysts. **2.** Photomicrograph of the sample above showing chlorite filling vesicles, miarolitic voids and veins, and replacing the groundmass; a glomerophytic aggregate of olivine microphenocrysts (lower left corner) is replaced by quartz, pyrite, chalcopyrite, and minor chlorite; two plagioclase microphenocrysts (upper right corner and center) are replaced by quartz and chlorite with minor pyrite. Uncrossed polars, field of view = 1.5 mm. **3:** 0.75-mm-thick quartz (along selvages) + pyrite (in center) vein in the sample above. Notice the screen of “dirty” quartz between two large pyrite crystal aggregates in the center of the vein, in the upper left corner. In the host rock, plagioclase microlites are mainly replaced by quartz with minor chlorite. **4.** Sample 158-957E-18R-1 (Piece 4, 20–24 cm) of a basaltic breccia formed by clasts which were initially chloritized, then paragonitized, silicified and pyritized. The clasts are cemented by a quartz + pyrite + paragonite matrix. Several dark green (dark gray in the photograph) chloritized angular clast cores are surrounded by light buff-colored paragonitized halos. The sample is crossed by several millimeter-sized quartz + pyrite veins and bordered, from top to lower left, by a 1-cm-thick pyrite + quartz vein. Notice in the triangular, dark gray, chloritized clast core, in center right, a 1-mm-thick, darker chlorite vein that continues, in the light buff halo on both sides, as a white paragonite vein (see next figure). **5.** Sketch illustrating the part of the chloritized clast core grading into a paragonitized halo in the sample described above. The early chlorite veins in the chloritized cores give way, in the paragonitized alteration halos, to paragonite veins that are themselves intersected by later pyrite + quartz veins. **6.** Photomicrograph of Sample 158-957E-18R-1 (Piece 5, 25–27 cm) of a silicified and paragonitized hyaloclastite with a chalcedony matrix and disseminated fine grained pyrite. In the dark, angular shards, the basaltic glass has been mainly replaced by chlorite, whereas in the light-colored shards, it has been replaced by paragonite. Two generations of quartz veins crosscut each other and intersect both clasts and matrix. Uncrossed polars, field of view = 6 mm.

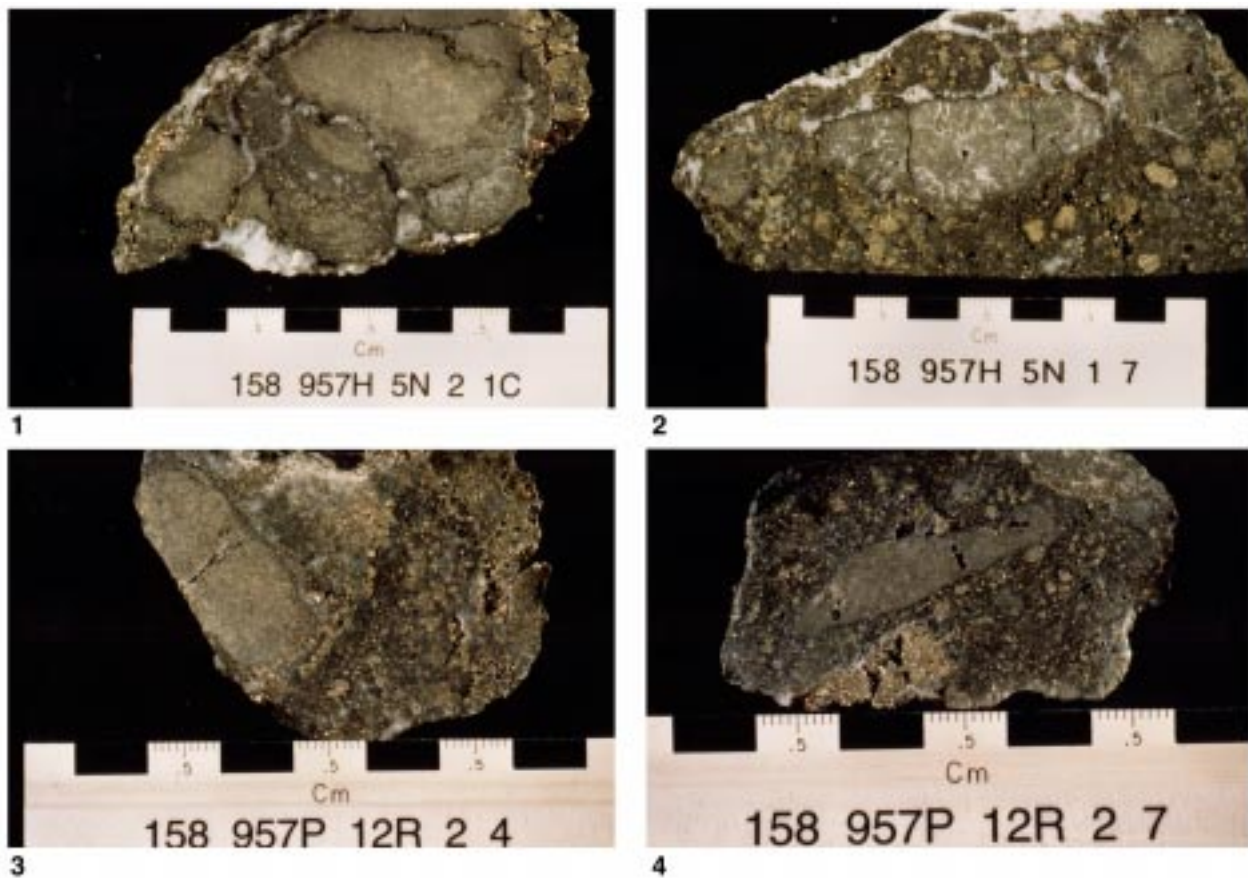
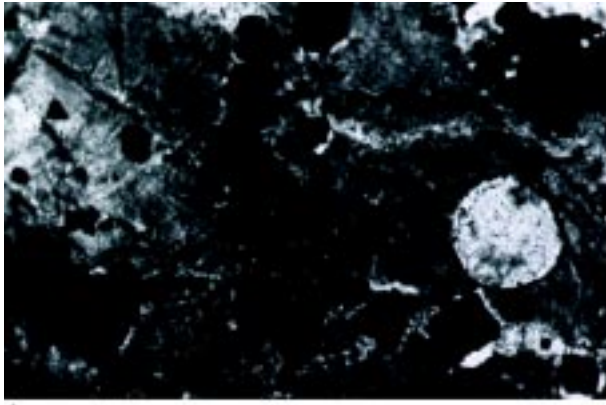
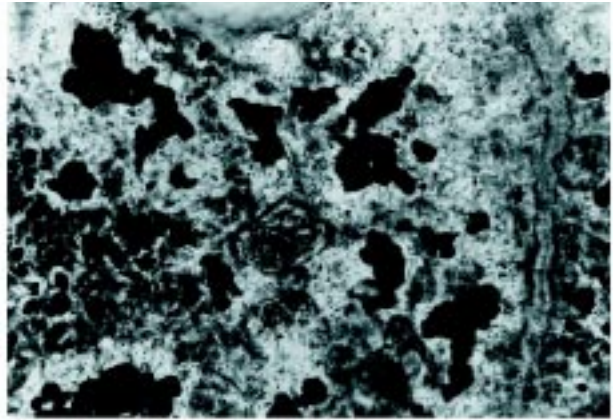


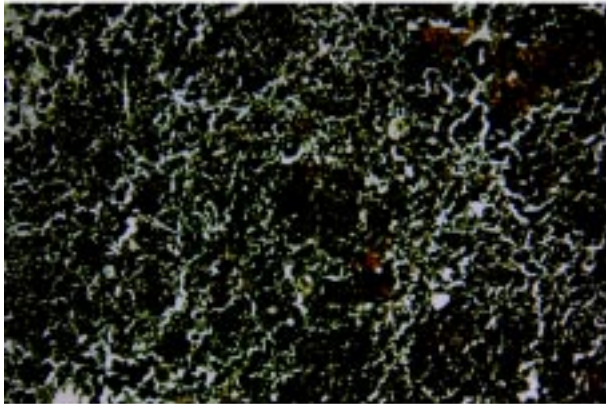
Plate 4. Photomicrographs of hand specimens of the “silicified wallrock breccia” (i.e., silicified, pyritized, and paragonitized stockwork) and the various types of “pyrite silica breccias” containing pervasively silicified, pyritized, and paragonitized basalt clasts. The basalt clasts illustrated range from subangular to subrounded in shape. **1.** Sample 158-957H-5N-2 (Piece 1C, 16–25 cm) from TAG-2 south distal area showing, in a stockwork sample, the “expansion” of the basalt clasts as a result of recurrent and pervasive hydrothermal replacements. Notice that several fragments belonging to the same clasts (e.g., center to upper right corner) are still contiguous. The white veins, ranging from 0.5 to 7.5 mm in thickness, are formed by late anhydrite. **2.** Sample 158-957H-5N-1 (Piece 7, 65–77 cm) from the same TAG-2 area, showing several hydrothermally altered basalt clasts in a “nodular pyrite silica breccia.” The clast at center, about 5.5 cm in length, exhibits two vertical open fractures and numerous millimeter-thick veins mainly filled with quartz. On the other hand, the thicker veins crossing the upper part of the sample and bordering it are formed by late anhydrite. **3.** Sample 158-957P-12R-2 (Piece 4, 16–20 cm) from the TAG-5 north distal area showing, along the left edge, a 3-cm-long, pervasively altered basalt clast in a “nodular pyrite silica breccia.” The basalt clast is cut by a late vuggy pyrite vein with minor quartz. **4.** “Nodular pyrite silica breccia” Sample 158-957P-12R-2 (Piece 7, 32–36 cm) from TAG-5 area showing a 3-cm-long hydrothermally altered basalt clast, in the center of the sample, and another one, about 2.5 cm long, along the upper right edge. In both samples shown in Figures 3 and 4, two generations of brecciation and cementation by quartz and pyrite are observed as the basalt clasts are intersected by a network of thin, quartz + pyrite veins and are cut by later pyrite veins. The clasts are enclosed in a matrix of dark gray silica with disseminated pyrite, which cements the smaller massive, granular pyrite clasts.



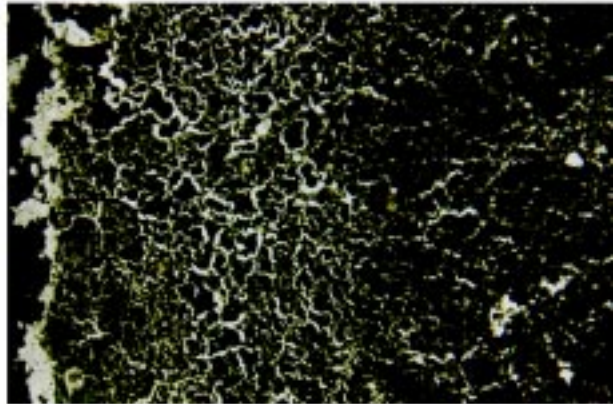
1



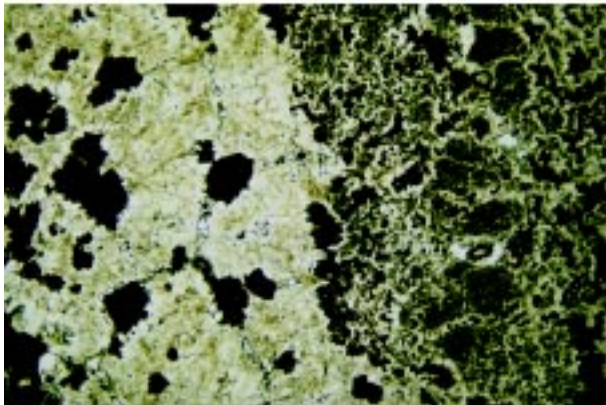
2



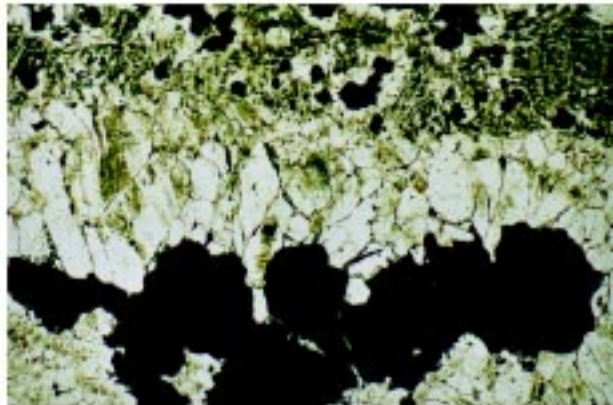
3



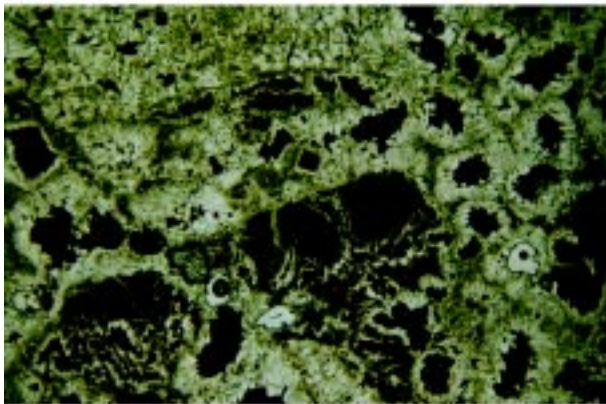
4



5



6



7



8



Plate 5. Photomicrographs illustrating the progressive silicification, pyritization, and paragonitization of the stockwork from beneath the central part of the mound. **1.** Euhedral pyrite crystals locally surrounded by quartz rims are disseminated in a silicified and argilized (both chlorite and paragonite are present) basalt clast in Sample 158-957E-14R-1 (Piece 11, 52–55 cm). The 150- $\mu\text{m}$  diameter vesicle, right center, is lined with a 10- $\mu\text{m}$ -thick layer of quartz and filled with fibroradial paragonite. The argilized groundmass displays a clear microlithic texture. A quartz + pyrite vein is observed in the upper left corner. Uncrossed polars, field of view = 1 mm. **2.** Basalt clast pervasively replaced by quartz + pyrite + paragonite in Sample 158-957C-16N-2 (Piece 3C, 34–36 cm). The primary subvariolic texture has almost completely been erased except in the lower left corner. Notice the quartz + pyrite + paragonite pseudomorph after an olivine microphenocryst (about 0.25 mm in length) in the center. Quartz appears “dirty” because of the numerous submicroscopic inclusions of paragonite and fluids. Uncrossed polars, field of view = 1.5 mm. **3.** Central part of a basalt clast in Sample 158-957E-14R-1 (Piece 5, 17–20 cm). The subvariolic texture is clearly visible and two plagioclase microlites, about 0.75 mm in length (e.g., upper left corner and just below center) have been replaced by quartz, whereas vesicles about 0.1 mm in diameter (e.g., near the microlite below center) were filled with paragonite. Euhedral pyrite crystals ranging from 0.02 to 0.25 mm on edge are disseminated throughout rock; they are often surrounded by 10- to 50- $\mu\text{m}$ -thick quartz coronas. In the upper right corner, notice the orange-brown (lighter gray in the figure) patch of groundmass that is less altered. Uncrossed polars, field of view = 6 mm. **4.** Area adjacent to a quartz + pyrite vein (along selvages and in center of the vein respectively), near the margin of the same clast. Near the vein, the pyrite crystals are more numerous and their quartz coronas merge into one another. Same sample, same conditions. **5.** Margin of a basalt clast grading into the quartz + pyrite matrix of “pyrite silica breccia” Sample 158-957C-14N-2 (Piece 1A, 10–13 cm). The subvariolic texture of the basalt is still visible in a series of 0.3- to 0.5-mm patches in the third part to the right of the figure. Uncrossed polars, field of view = 15 mm. **6.** The subvariolic texture has almost completely disappeared from the margin of a basalt clast as it was replaced by festoons of merging pyrite with quartz coronas (upper half) and graded into the pyrite + elongated quartz crystal matrix (lower half). Notice that the matrix quartz is often “dirty” in the parts farther away from the contacts with the pyrite. Sample 158-957C-16N-1 (Piece 16, 134–137 cm). Uncrossed polars, field of view = 6 mm. **7.** The basalt clast(s) in “pyrite silica breccia” Sample 158-957E-4R-1, (Piece 3, 12–14 cm) has (or have) been almost completely replaced by quartz + pyrite + paragonite. Only two relicts, about 5 and 3 mm in diameter, displaying faint subvariolic textures are observed in lower center and in lower left corner. They are crossed by festoons of quartz (along selvages) + pyrite (in center) veins. The breccia matrix is a mosaic of isolated euhedral pyrite crystals (e.g., near center), or pyrite aggregates surrounded by clear quartz crystals coronas grading into “dirty” interstitial quartz. Uncrossed polars, field of view = 15 mm. **8.** Any trace of primary basaltic texture has disappeared from all of the other parts of the sample of “pyrite silica breccia” above. Most of this sample is made up of often large pyrite aggregates surrounded by an elongated quartz crystal corona grading into “dirty” quartz with interstitial paragonite. Uncrossed polars, field of view = 6 mm.

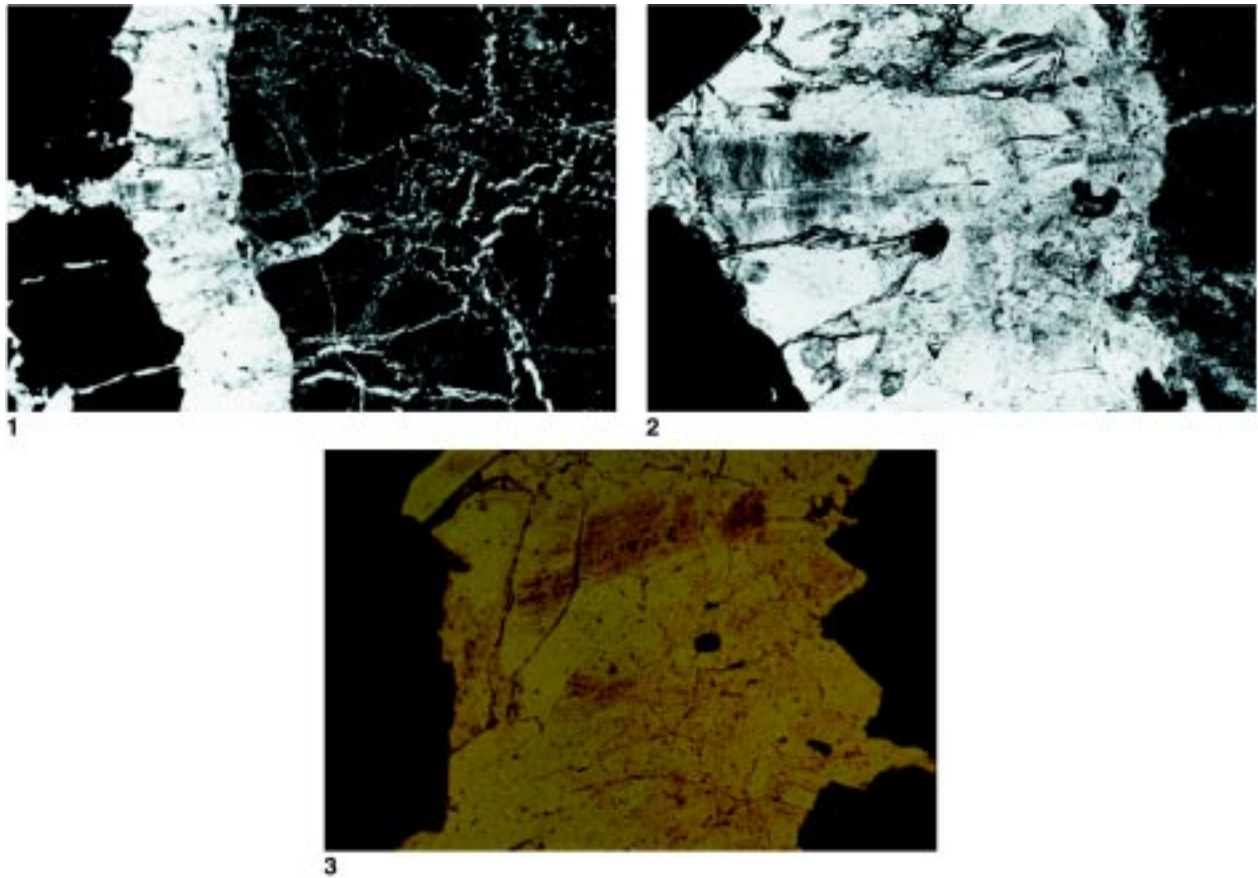


Plate 6. "Dirty" quartz in "wallrock silicified breccia," (i.e., silicified, pyritized, and paragonitized stockwork from beneath the central part of the mound). **1.** Photomicrograph of Sample 158-957E-14R-1 (Piece 11, 52–55 cm) shows, on the right, the margin of an altered basalt clast with sub-variolitic texture and criss-crossed by numerous quartz + pyrite veinlets (less than 0.5 mm thick); and, on the left, a 2-mm-thick quartz + pyrite vein in the center, whereas elongated quartz crystals up to 0.6 mm long and perpendicular to the clast rim form its selvages. The vein quartz crystals are often "dirty" because of numerous paragonite and fluid inclusions. The large quartz crystals with the distinctive pattern of inclusion trails, extending through the middle of the pyrite vein, on the left, are magnified in the next figure. Uncrossed polars, field of view = 6 mm. **2.** Detail of the vein quartz from the preceding figure (i.e., "dirty" quartz at center, rim of the basalt clast on the right, and vein pyrite on the left) showing the trails of inclusions in two adjacent "dirty" quartz crystals (center left). This inclusion pattern is similar in size and shape to the subvariolitic textures of the basalt clasts. The other quartz crystals forming the vein contain numerous but randomly distributed inclusions. Uncrossed polars, field of view = 1.5 mm. **3.** Similar trails of inclusions cutting across several large, elongated "dirty" quartz crystals in a quartz + pyrite vein in Sample 158-957C-16N-1 (Piece 16, 134–137 cm). Uncrossed polars, field of view = 1.5 mm.

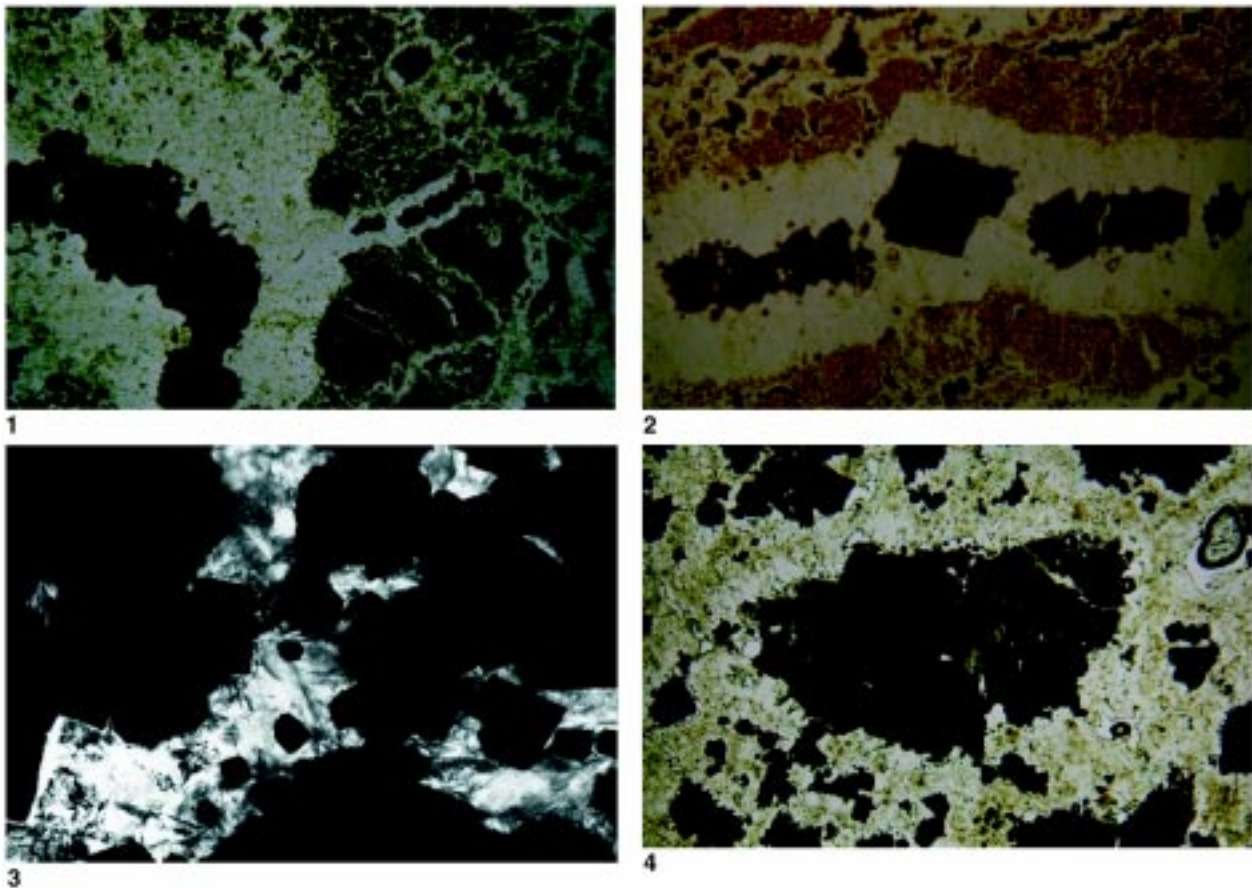
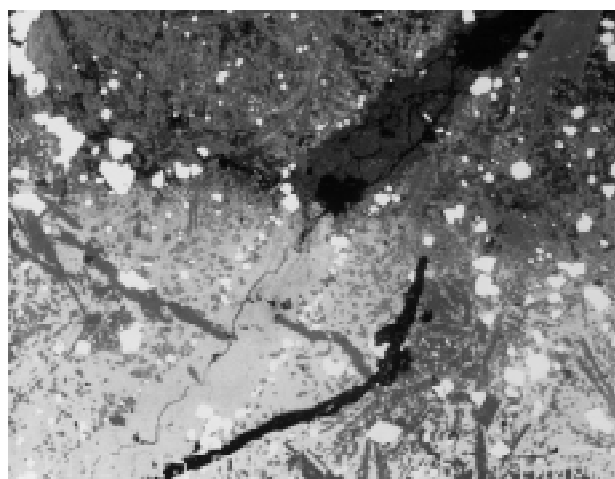
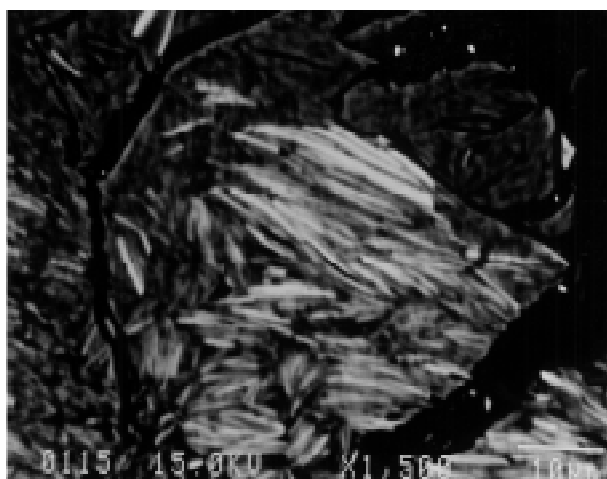


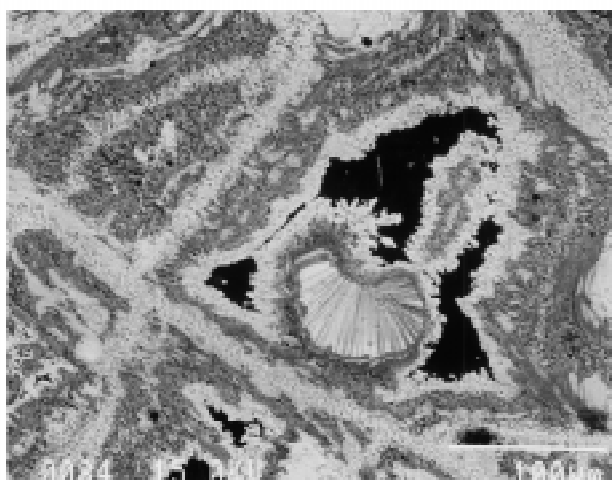
Plate 7. Photomicrographs of veins in silicified, pyritized, and paragonitized clasts in the hydrothermally altered stockwork, and interstitial occurrences of paragonite in the completely replaced clasts and in the pyrite + quartz + paragonite matrix of the “pyrite silica breccias.” **1.** Veins of pyrite (in center) and quartz (along selvages) in the rim of an “expanded” basalt clast (right half of the figure) in a “pyrite silica breccia” from the silicified, pyritized, and paragonitized stockwork beneath the central part of the mound (Sample 158-957C-16N-2 (Piece 3C, 34–36 cm). The veins range from 0.05 to 0.6 mm in thickness. Compare the paragenetic similarity of the veins with the large pyrite aggregate surrounded by a quartz corona forming the breccia matrix (left half of the figure): the intraclast veins appear to merge into the matrix. Notice, in center, the poorly defined boundary between the basalt clast and the matrix. Uncrossed polars, field of view = 6 mm. **2.** A 2.5-mm-thick vein of quartz (along selvages) and euhedral pyrite crystals or crystal aggregates (at center) crosses through a silicified, pyritized, and paragonitized basalt clast in Sample 158-957E-17R-1 (Piece 3, 18–22 cm). Subparallel thinner quartz + pyrite-festooned veins are observed in the host basalt clast on either side of the thicker vein. Notice that the 0.5-mm-thick elongated quartz crystal corona surrounding the large (i.e., 1.5 mm on edge) euhedral pyrite crystal, at center, mimics the cubic shape of the pyrite crystal. Uncrossed polars, field of view = 7.5 mm. **3.** Numerous paragonite flakes forming sheaf-like aggregates (up to 50  $\mu\text{m}$  in length) disseminated in “dirty” anhedral quartz that is interstitial among aggregates of euhedral pyrite crystals replacing a completely pyritized, silicified, and paragonitized basalt clast in “pyrite silica breccia” Sample 158-957I-1N-1 (Piece 12, 75–76 cm) from the distal TAG-4 west area. Uncrossed polars, field of view = 1.5 mm. **4.** Showing an interstitial phyllosilicate—paragonite and/or chlorite (dark gray, in center of figure)— among the subhedral crystals of a pyrite aggregate surrounded by a “dirty” quartz corona. Sample 158-957C-14N-2 (Piece 1A, 10–13 cm) of silicified, pyritized, and paragonitized stockwork from the central part of the mound TAG-1 area.



1



2



3

Plate 8. Backscattered electron photomicrographs of chlorite replacement by paragonite in Sample 158-957E-18R-1 (Piece 4, 20–24 cm). Dark areas are poorer in Fe and lighter areas are richer in Fe. **1.** Reaction front showing replacement of chlorite by paragonite. Rock in lower half of photo consisting of chlorite (light gray), quartz (gray), and pyrite (white) is replaced in upper half by paragonite (dark gray), quartz (gray), and pyrite (white). The reaction is strikingly visible in the center of the photo, where the 25- $\mu$ m-wide chlorite vein (light gray) running from the lower left to upper right has been transformed into paragonite (dark gray) at the upper right. **2.** Close-up of reaction front within vein from Figure 1. Chlorite laths (light gray) are enclosed within and are being replaced by surrounding paragonite. Analyses of this chlorite reveal higher Fe/Fe+Mg, Si, Na and total interlayer cations than chlorite farther from the reaction front, suggesting partial equilibration with hydrothermal fluids and that paragonite layers are present within the chlorite at a scale finer than can be detected in the photograph. **3.** Backscattered electron photomicrograph of portion of plagioclase phenocryst replaced by chlorite in Sample 158-957E-18R-1 (Piece 1, 4–7 cm). Microprobe analyses of these different zones are shown in Figure 7 and illustrate extreme compositional variation on a scale of tens of micrometers.